

Opposing transcriptomic gradients explain orthogonal maps in human visual areas

Zonglei Zhen^{*1,2}, Jesse Gomez^{*3,4}, Kevin S. Weiner^{3,4}

1. Beijing Key Laboratory of Applied Experimental Psychology, Beijing Normal University, Beijing, China
2. Faculty of Psychology, Beijing Normal University, Beijing, China
3. Helen Wills Neuroscience Institute, University of California Berkeley, Berkeley, California, United States of America
4. Psychology Department, University of California Berkeley, Berkeley, California, United States of America

* These authors contributed equally

Abstract

Opposing transcriptomic gradients explain the large-scale organization of cortex. Here, we show that opposing transcriptomic gradients also explain the fine-scale organization of orthogonal maps in human visual areas. We propose a model relating transcriptomics, cell density, and function, which predicts that specific cortical locations within these visual maps are microanatomically distinct and differentially susceptible to genetic mutations. We conclude with histological and translational data that support both predictions.

Main Text

Active transcription of a small set of genes contributes to the large-scale realization of functional hierarchies and gradients in human cortex. Two recent studies reveal that both the broad layout of functional regions¹ and even the hierarchical ordering of regions within a processing stream² are accurately described by genetic transcription that produces opposed, linear gradients in cortex. However, whether this broad relationship extends to smaller spatial scales is unknown. Thus, the goal of the present study was to answer the following fundamental question: *What role do genes play in the organization of functional gradients, or topographic maps, within a single human cortical area?*

While genetic gradients (e.g., Ephrins) during gestation establish the topography of connectivity in visual cortex³, the role that additional genes play in the layout of topographic maps within cortical areas in the adult brain is less well understood. To fill this gap in knowledge, we employed a dataset⁴ detailing the transcriptomic landscape of adult human cortex from the Allen Human Brain Atlas (AHBA). Early visual areas (V1, V2, V3) were used as target areas because they contain two, well-characterized orthogonal maps of eccentricity and polar angle⁵ (Fig 1a) that can be modeled in the absence of functional data⁶. Using tools from our previous work², tissue samples and functional areas were aligned to the same cortical surface.

We tested the *a priori* hypothesis that opposed linear gradients are not only a feature employed by cortex at the large-scale^{1,2}, but also at finer spatial scales within

cortical areas. We identified tissue samples ($n=136$) from the AHBA located within human early visual areas that form linear gradients correlated with eccentricity or polar angle. To minimize false alarms, we selected only the top 1% of positively and negatively correlated genes ranked by the negative log of their p-values as in previous work². Example genes whose expression correlated positively (higher expression in periphery) or negatively (lower expression in periphery) with increasing eccentricity are illustrated in Fig 1b. In each area, we observe significant correlations ($r's > 0.6$, $p's < 0.001$) between the magnitude of genetic transcription and either polar angle or eccentricity, suggesting that the orthogonal maps of receptive field (RF) properties are described by equally orthogonal genetic gradients, which is consistent with our hypothesis. All correlations were between 29.5 and 40.2 standard deviations above their respective bootstrapped ($n=1000$) null distributions (gray line in Fig 1c-d; Online Methods).

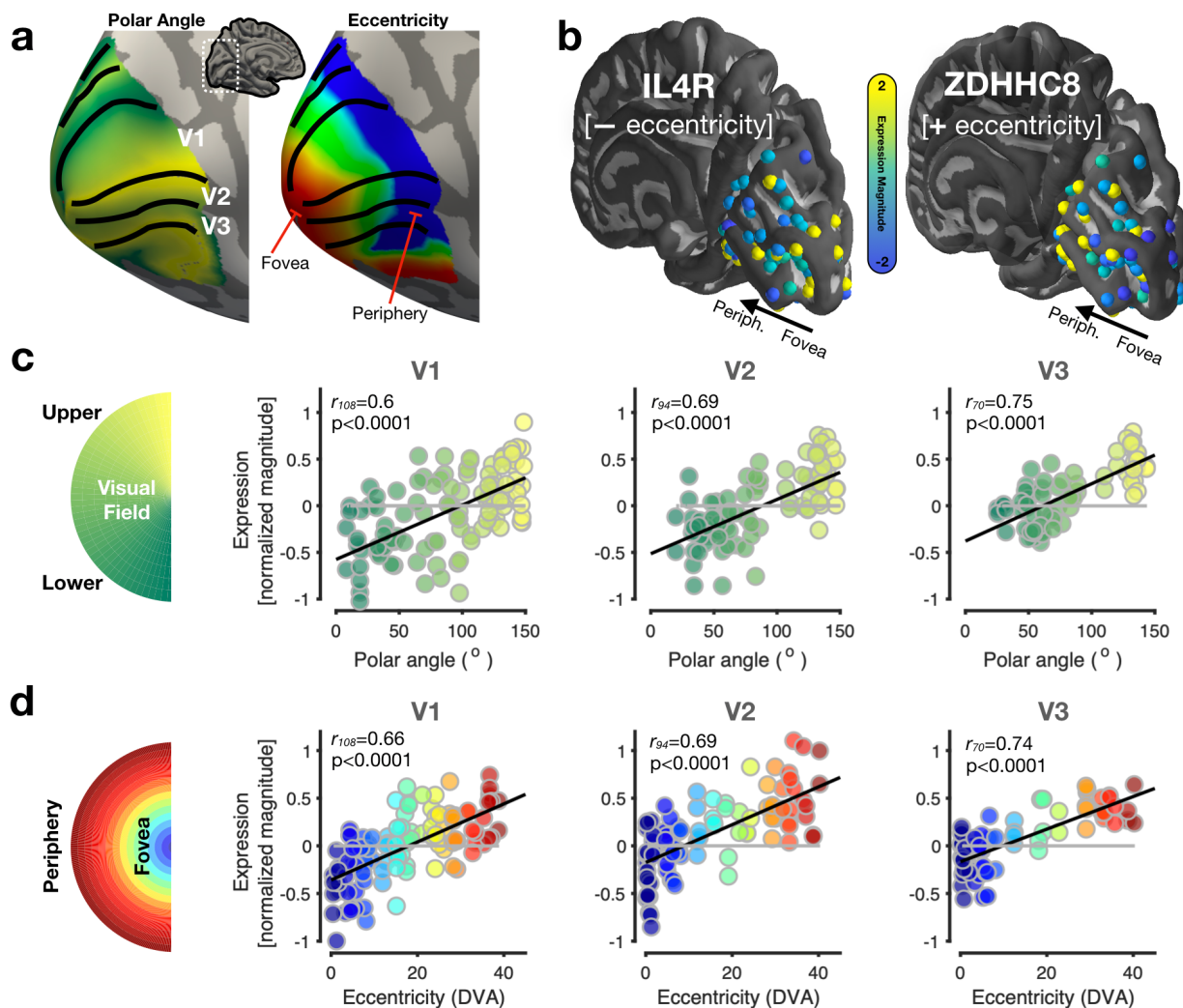


Figure 1: Opposing transcriptomic gradients explain orthogonal maps in human visual areas. (a) Example orthogonal maps of polar angle and eccentricity on an inflated cortical surface. Areas V1, V2,

and V3 are defined (Online Methods). **(b)** Right hemisphere tissue samples of the AHBA projected onto the cortical surface. Inset bar displays colormap of normalized expression magnitude. Example genes whose transcription levels form either a negative gradient (left) or positive gradient (right) in relation to eccentricity. **(c)** Correlations between a tissue sample's polar angle preference and the mean expression of the top 1% of genes. For illustration purposes, the positive and negative gradients have been combined by inverting the sign of the negative gradient. As illustrated in Fig S1, the same result occurs when calculating correlations separately for each gradient. Black line: Line of best fit. Gray line: Average correlation from a bootstrapping ($N=1000$) procedure in which genes were randomly selected (Online Methods). **(d)** Same as (c) but for the underlying eccentricity value of each tissue sample. DVA: degrees of visual angle.

Interestingly, the identified genes are largely area- and map-specific. When calculating the dice coefficient between the genes contributing to the layout of eccentricity and polar angle within each area, there is little (~3%) overlap (dice of V1: 0.12; V2: 0.07; V3: 0.07; see Fig S2 for overlap between areas). The identified genes (Table S1) are independent of those identified previously that contribute to the large-scale arealization of the visual processing hierarchy (Fig S2), indicating that cortical organization employs linear transcription gradients at multiple spatial scales using unique sets of genes. Additionally, polar angle and eccentricity measurements of one area (e.g., V1) do not predict ($-0.33 < r's < 0.34$, $p's > 0.05$; Figs S3-S6) the gene expression in another area (e.g., V2 or V3).

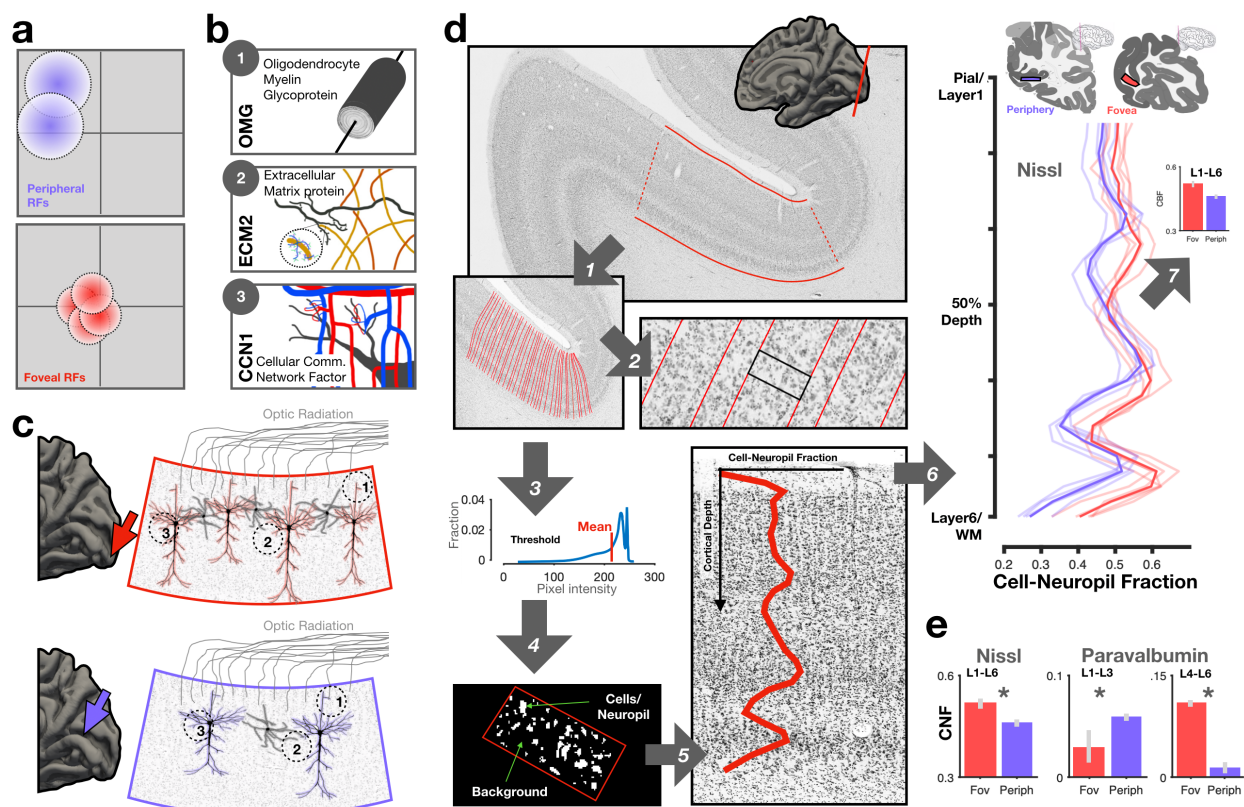


Figure 2: Validating tissue differences between foveal and peripheral cortex predicted by a functional-genetic model. (a) Schematic showing that receptive fields (RFs) are denser and smaller in

foveal (red) compared to peripheral (purple) cortex. **(b)** Identified genes with increased expression in foveal compared to peripheral cortex (Table S1) suggests that higher RF density in foveal cortex is associated with higher expression of genes that regulate macromolecular tissue structures such as myelin (OMG), extracellular matrix material (ECM2; collagen, yellow curves; glycoproteins (blue/purple inset), and capillary junctions (CCN1). **(c)** A functional-genetic model resulting from (a) and (b) hypothesizes that higher RF density and increased expression of genes controlling key tissue structures will result in higher cellular/neuropil density in foveal cortex (posterior calcarine sulcus, red arrow) compared to peripheral (anterior calcarine sulcus, purple arrow). Right: Schematic illustration of cellular/neuropil density differences between foveal (top) and peripheral (bottom) cortex. Colors: neurons. Gray: interneurons. Dotted circles (1-3): Where proteins of the genes in (b) are likely localized. **(d)** Basic steps of the approach developed here to quantify cytoarchitecture from coronal Nissl stains, which derives the fraction of pixels above background which we deem cell-neuropil fraction (CNF) along cortical traversals modeled to follow the organization of cortical columns. See Online Methods for description of the pipeline resulting in average CNF measurements across cortical layers (upper right inset) and histological slices. Red: foveal; Purple: peripheral slices of pericalcarine cortex. Dark contours represent the mean (step 6). Upper insets indicate the location of the histological slices from which each ROI (colored rectangles) was defined. **(e)** Left: Bar graph indicates that foveal portions have a significantly higher ($p < 0.005$) CNF (0.52 ± 0.02) compared to peripheral portions (0.45 ± 0.02) from Nissl stained sections. Right: Control analyses of parvalbumin stains show that CNF varied by cortical layer (Layers 1-3, peripheral > foveal, $t(8)=2.72$, $p < 0.03$; Layers 4-6, foveal > peripheral, $t(8)=5.2$, $p < 0.001$) indicating that foveal and peripheral cortical slices do not always vary by a global mean difference simply as a result of potential processing biases of the histological tissue (Online Methods).

The latter finding is particularly surprising considering that the representation of eccentricity is shared across areas V1-V3. We hypothesized that the identified genes may have different roles in the development of features that contribute to functional differences between areas and within a given topographic map. Two parsimonious features fit these criteria. Firstly, RFs are smaller and denser in foveal compared to peripheral cortex, as well as smaller in V1 compared to V2 and V3 (Fig 2a)⁷. Secondly, negative eccentricity gradient genes code for many microstructural proteins (Fig 2b) whose expression also decreases from fovea to periphery. Together, denser RFs and microstructure-promoting transcription generate a functional-genetic model (Fig 2c) that makes the explicit prediction that human foveal cortex has an increased density of cells and relevant neuropil to support the increased fidelity of vision associated with foveal processing. Employing a new histological quantification approach (Fig 2d), we successfully demonstrate differences in cell/neuropil density between foveal and peripheral V1 (Fig 2d, 2e) for the first time in humans, which is consistent with measurements from non-human primates⁸.

This functional-genetic model also makes the translational prediction that mutations in a subset of the identified genes should produce specific visual field deficits, likely unevenly across a given map. We verify the feasibility of this prediction with CXorf58 (Fig 3), an X chromosome gene whose expression negatively correlated with eccentricity and has been linked to retinitis pigmentosa (RP), which results in perceptual deficits of the peripheral visual field. Mutations in CXorf58 may also explain recent findings⁹ showing that females with Turner Syndrome (TS) — a condition in which an X chromosome is damaged or missing¹⁰ — present with deficits in RF coverage of the peripheral visual field specifically in V2 and V3, where CXorf58 is

negatively correlated with eccentricity (Fig 3). Additional mutations in SLTRK4 and RAI2 — both X chromosome genes involved in axonogenesis¹¹ and cell growth¹² and identified here — could adversely impact peripheral representations where tissue microstructure reductions would hinder the fidelity of neural circuits underlying the pooling of visual information.

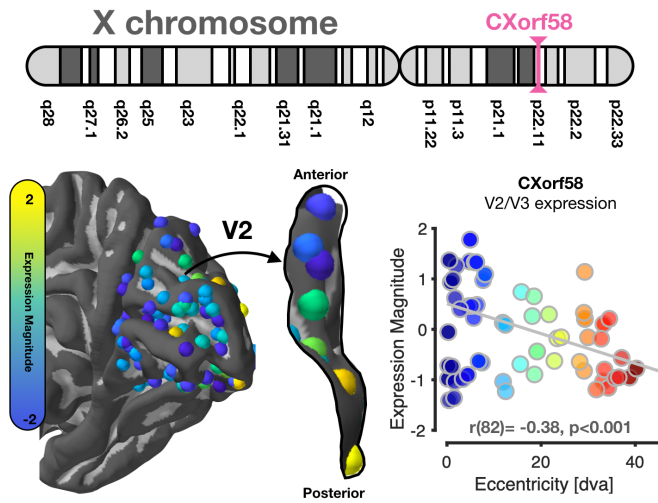


Figure 3: Translational insights into the role of genetic mutations in the loss of peripheral vision. The functional-genetic model makes the translational prediction that mutations in a subset of the identified genes should produce specific visual field deficits. *Top:* The location of CXorf58 on the short arm of the X chromosome. Mutations in CXorf58 have been linked to retinitis pigmentosa (RP), which results in peripheral vision deficits. *Bottom left:* Expression pattern of CXorf58 within the human occipital lobe. Expression within dorsal V2 is emphasized given recent findings showing that patients with Turner syndrome have reduced peripheral visual field coverage in V2 and V3 compared to controls. *Bottom right:* Expression pattern of CXorf58 negatively correlates with eccentricity.

correlates with eccentricity. We propose that CXorf58 mutations may not only be linked to deficits associated with RP, but also Turner syndrome.

Altogether, our results suggest a new rule of cortical organization in which the adult brain employs opposed transcriptional gradients at multiple spatial scales: across the cortex¹, across areas within processing hierarchies², and now across maps within a single area. Previously, we hypothesized that large-scale transcription gradients contributed to the differences in population RFs across areas of the visual processing hierarchy. Here, we improve the resolution of this hypothesis by an order of magnitude to the anatomical scale of cellular structures and the functional scale of RFs within a single visual map. While transcriptomic gradients contribute to the layout of RF properties within and across field maps, additional evidence suggests that such transcription shows protracted development², and that RFs are even sculpted through experience and viewing behaviors¹³. Thus, experience likely modulates the transcription of genes involved in structural mechanisms underlying RFs. Future work will add additional features such as connectivity³ and cortical layering¹⁷ to the present model, which will continue to deepen our understanding of the balance between transcriptomic and experiential contributions to the structure and function of human cortex.

Online Methods

Data

All analyzed data were curated from the following open datasets:

- 1.Allen Human Brain Atlas (AHBA) Microarray Data: <http://human.brain-map.org>
- 2.Neuropythy atlas of human visual cortex: <https://github.com/noahbenson/neuropythy>
- 3.BrainSpan histological stains: <http://www.brainspan.org/static/atlas>

Defining eccentricity and polar angle maps in areas V1, V2, and V3

Human visual areas are defined by two orthogonal functional maps: one of a receptive field's (RF) polar angle describing its polar position along the circular image of the retina, and one of eccentricity, describing its distance from the center of the visual field (the fovea). While maps of eccentricity are shared across early visual areas, the transition of one area to another is based on differences in polar angle⁵. Polar angle transitions between early visual areas occur with such regularity relative to the folding of cortex that a model based on an individual's cortical anatomy is sufficient to automatically define areas V1 through V3 as precisely as manual definitions of these areas⁶. We applied this model to a cortical surface of the MNI152 brain, which is an anatomical average of human cortex from the Montreal Neurological Institute made from the average of 152 brains. This cortical space was chosen given that tissue samples from the donor brains of the AHBA have been aligned to the same MNI volumetric space. A cortical surface was produced for this anatomical volume using FreeSurfer¹⁴.

AHBA Tissue Samples

The AHBA provides transcription data across human cortex, pooled from six donors and processed via Microarray. Microarray samples underwent strict normalization and data quality checks through AHBA as described here: <http://human.brain-map.org>. For data organization, preprocessing was identical to our previous work². Importantly, we follow the standardized processing pipeline proposed by Arnatkeviciute, Fulcher, and Fornito¹⁵. Briefly, the raw microarray expression data for each of the six donor brains included the expression level of 29,131 genes profiled via 58,692 microarray probes. We implemented five preprocessing steps. First, probes were excluded that did not have either a) a gene symbol or b) an Entrez ID. This resulted in 20,737 genes. Second, the expression profiles of all the probes targeting the same gene were averaged. Third, in order to remove variability in gene expression across donors, gene expression values of tissue samples were normalized by calculating z-scores separately for each donor. Fourth, because previous studies did not identify significant inter-hemispheric transcriptional differences, data from both hemispheres were combined. Finally, comparing a tissue sample's genetic expression to either the eccentricity or polar angle of its underlying cortex required mapping these tissue samples to a common cortical space. Each sample from the AHBA was

associated with a 3D coordinate from its donor's MRI brain volume and its corresponding coordinate (x , y , z) in the MNI152 space. Each tissue sample was mapped to the nearest cortical surface vertex with a 5mm distance threshold and assigned to the visual field map in which that surface vertex was contained. This resulted in the following number of tissue samples aligned to each visual area: 54 in V1, 47 in V2, and 35 in V3.

Comparing gene transcription and visual field map properties

With tissue samples and maps of eccentricity and polar angle having been mapped to the same cortical surface, we extracted the underlying eccentricity or polar angle from each tissue sample by taking the average of the vertices that were within a one voxel radius of the vertex to which the tissue sample had been mapped. As our previous study identified that genes distinguishing regions along a cortical processing hierarchy are organized into opposed, linear gradients², we first tested the *a priori* hypothesis that opposed gradients would also exist within a single brain region to explain the orthogonal maps of eccentricity and polar angle of visual field maps. To that end, for each gene, we calculated the Pearson correlation between its expression magnitude across tissue samples within an area versus the mean eccentricity or polar angle of each tissue sample. Genes were then ranked by the negative log of their resulting p-values. As in the previous study², the top 1% of positively correlated and the top 1% of negatively correlated genes were kept. The average expression value of those top genes are illustrated in Fig 1. This was done separately for each visual field map. For example, the mean expression of the top 1% ($n=200$) of positively correlated genes in V1 is averaged within each tissue sample and then plotted against its eccentricity or polar angle (pink circles of Fig S1). For purposes of visualization, we combined the two gradients together into a single gradient by flipping the sign of the negative gradient for Fig 1, but the opposed gradient with their original signs are shown in Fig S1. A list of the top positive and negative gradient genes for eccentricity and polar angle are listed in Table S1 for each visual field map. By averaging across the top genes, we aim to capture a general pattern that is shared across many genes, rather than focusing on a single gene which is likely more susceptible to a Type II error. As a control analysis, we sought to generate a null distribution for each correlation using a bootstrapping approach. Across $n=1000$ bootstraps, we repeated each correlation in each field map but randomly selected the same number of genes as the main correlation (from the total population of 20,737 genes). We plot the averaged correlation in Fig 1 as gray lines for each field map. We calculated, in units of standard deviation, the distance that the main correlations were from the bootstrapped null distribution. These distances were very large, ranging from 29.5 to 40.2 standard deviations, underscoring the significance of the observed correlations.

Comparing inter-regional and intra-regional gene expression

In a previous study², we identified $n=200$ genes that formed opposed positive ("ascending") and negative ("descending") gradients along the visual processing hierarchy of occipito-temporal cortex. We hypothesized that given that these genes were identified as those that distinguish regions within a processing stream, they

should be unique, or non-overlapping, with the genes identified in the present study that are correlated with functional topography within a visual area. From these 200 inter-regional genes, and the intra-regional genes identified in each field map (2 orthogonal maps * 2 gradients * 200 genes per gradient = 800 genes per field map), we calculated the dice coefficient to describe the overlap of these two sets per field map. The dice coefficient (DC) is calculated as twice the number of overlapping genes normalized by the size of both lists. In this way, the highest DC possible for the dataset at hand is 0.5. The resulting DC for this analysis for V1, V2, and V3 is shown in Fig S2a. Of these 1000 total genes going into the DC analysis, approximately 2 overlapped. We also repeated this analysis for the list of intra-regional genes identified in two visual field maps. The resulting three DCs from the possible combination of comparisons for the three visual field maps is shown in Fig S2a. Next, to explicitly validate that the inter-regional genes identified in the previous study were not correlated with eccentricity or polar angle, separately for each of the “ascending” and “descending” gene gradients, we correlated the mean expression of these genes in the current tissue samples with eccentricity and polar angle in V1, V2, and V3. All of the resulting 12 correlations illustrated in Fig S2b were indeed non-significant: $-0.2 < r's < 0.22$, $p\text{-values} > 0.18$. Lastly, we wanted to explicitly test if the genes identified from one region were correlated with functional properties in another region (Figs S3-S6). To do this, for example, we took the genes correlated with eccentricity in V2 and V3, removed the shared genes with V1 (e.g., genes that were also correlated with eccentricity in V1 were excluded) and then we correlated the expression of these unique V2/V3 genes in tissue samples of V1 with their underlying eccentricity. For all cases, we find no correlation (Bonferroni correction for multiple comparisons) with the exception of V2-unique genes being correlated with eccentricity in the tissue samples of V1.

Quantifying histological slices of human cortex with BrainWalker

In order to test the feasibility of the hypothesis that gene transcription differences between foveal and peripheral representations within a single visual field map might induce microanatomical differences in the underlying cortical sheet, we developed a method to quantify human cytoarchitecture that a) was repeatable across different histological samples, b) could capture anatomical variation across cortical layers, and c) was importantly, observer-independent. To achieve this goal, we developed an analysis pipeline called BrainWalker that quantifies the fraction of cell bodies and neuropil (cell-neuropil fraction, CNF) above background noise in a given histological stain. Importantly, this software slides or “walks” across cortical layers and columns, producing a vectorized description of the CNF for a desired piece of cortical ribbon. The software works as follows, and is illustrated in Fig 2d. First, the user selects a ribbon of cortex to be quantified, tracing the middle of Layer 1 of cortex, and the corresponding length of the gray-white matter boundary (Fig 2d, box 1). The two boundaries are then split into 200 equally spaced points. Points in Layer 1 and the white matter boundary are modeled as positive and negative electric charges, respectively, and then equipotential lines are drawn connecting each corresponding point on the two boundaries (Fig 2d, arrow 1). These equipotential traversals are meant to model the shape of cortical columns traversing the cortical sheet, importantly fanning at gyral crowns¹⁶. Each traversal is then split into 30 equally spaced points,

and then a window slides between two neighboring traversals along these 30 bins (Fig 2d, arrow 2). The underlying image (e.g., a Nissl stain) is thresholded at the mean pixel value to identify the “peaks” or puncta associated with cell bodies and neuropil structures (Fig 2d, arrow 3). While this threshold was somewhat arbitrary, a threshold was necessary to exclude irrelevant image structures such as holes from veins, tears in the tissue, or air bubbles on the mounting slide. These irrelevant values, or “background”, where the white slide mount becomes visible can be seen as the large peaks in the histograms of Fig S8. Fig S8 also shows that the chosen threshold does not impact the interpretation of the findings: histograms of all pixel values from the foveal and peripheral slices indicate that foveal slices (red) have greater tissue content at the entire range of lower pixel values corresponding to cortical tissue all the way up to the mean pixel intensity (solid black line) which marks the beginning of brighter pixels representing the slide background. Differences between foveal and peripheral slices at these higher pixel intensities result simply from the cropping of the images; foveal slices had more of the underlying slide visible as the posterior slices of the occipital pole were smaller than more anterior slices. After this thresholding, at every bin, the CNF (fraction of pixels belonging to cell bodies and neuropil versus background) is quantified (Fig 2d, arrow 4). The 30-bin vector for each traversal is then averaged across traversals, producing an average CNF contour detailing CNF from Layer 1 of cortex to white matter (Fig 2d, arrow 5). In Fig 2d, an example CNF contour is overlaid on a Nissl-stained section of human V1; one can appreciate how the peaks and valleys of the CNF contour highlight the different cell body densities across and between layers.

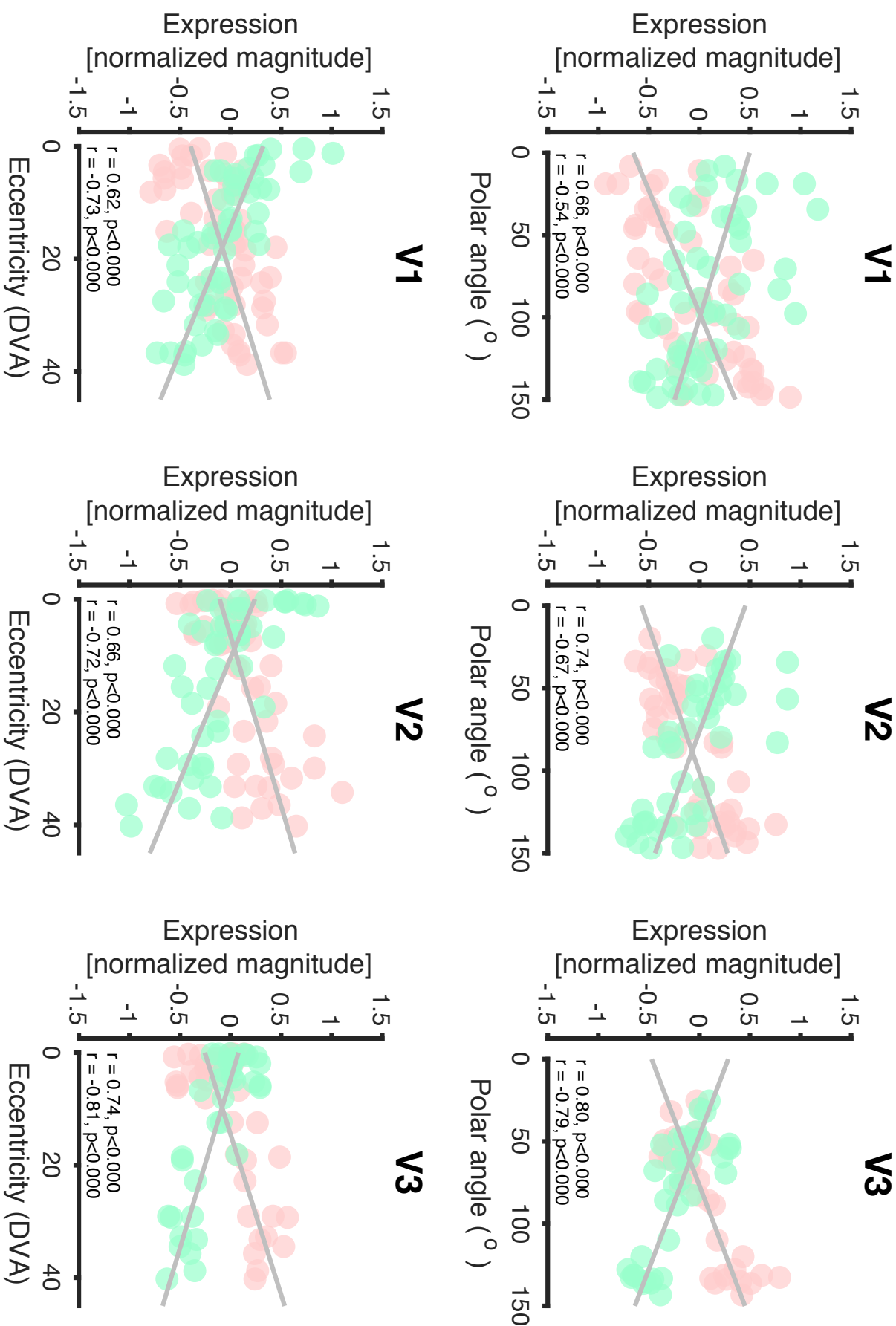
To generate CNF contours from human visual cortex, we used the freely available, high-resolution, Nissl-stained and Paravalbumin-stained coronal slices of human visual cortex from the Allen Institute’s BrainSpan Atlas (<http://www.brainspan.org/static/atlas>). In order to compare foveal and peripheral cortex, where genetic transcription is most differentiated in the present data and resulting anatomical differences are likely to be largest, we extracted slices (n=5) from the posterior Calcarine sulcus where foveal representations are located, and slices from the anterior Calcarine sulcus where the peripheral visual field is represented. To ensure that differences in overall stain intensity would not bias results, and to mirror the normalization steps for the transcriptional data, each slice was normalized by the mean pixel value of all the neighboring white matter pixels. On a region of the cortical ribbon spanning 1.25 centimeters, we extracted the CNF of each slice from V1 and plotted the CNF of each slice in Fig 2 comparing fovea and periphery for Nissl-stained cortex. We repeated this analysis with paravalbumin-stained cortex in Fig S6 (Fig 2e). For Nissl stains, we computed a simple two-sample t-test comparing the CNF between foveal V1 and peripheral V1 averaged across cortical layers (Fig 2e). For the paravalbumin stains, CNF varied by cortical layer, and t-tests were run comparing Layers 1-3 and Layers 4-6 separately (Fig 2e). Paravalbumin was analyzed not only as an additional feature that could vary by eccentricity, but as a control to ensure that foveal and peripheral cortical slices do not always vary by a global mean difference simply as a result of potential processing biases from the AHBA.

Intra-regional genes on the X chromosome

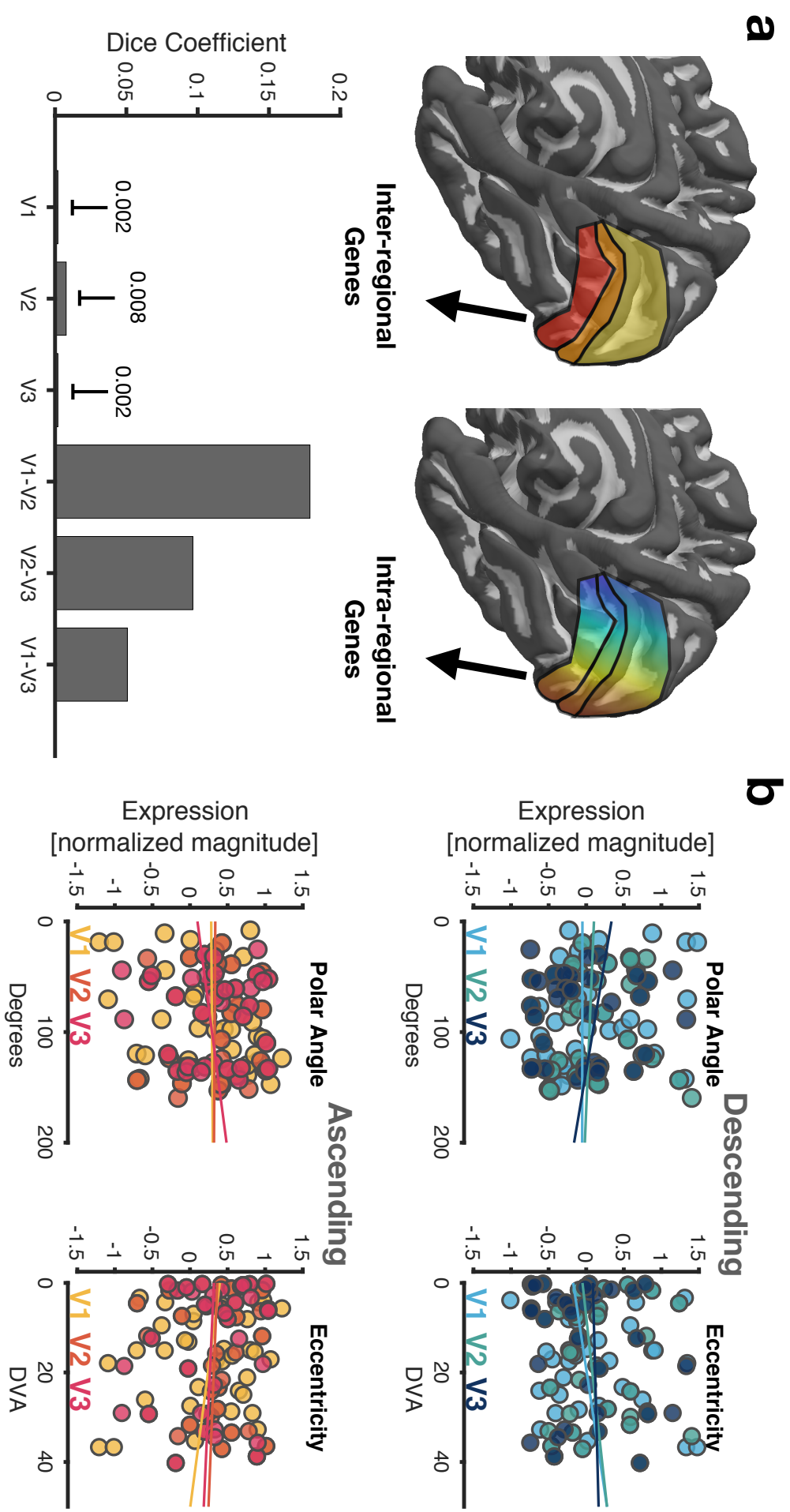
Turner syndrome is a condition affecting females in which the individual is either missing an X-chromosome (monosomy X) or one of the X-chromosomes is damaged. While the condition is hallmark by a number of physical atypicalities, genes on the short arm of the X chromosome (e.g., short stature homeobox gene, SHOX) have been linked to the stunted bone and limb growth that characterizes the small stature of those with Turner syndrome. Recent research has demonstrated that females with Turner syndrome present with visual deficits in the coverage of the periphery⁹. Retinotopic mapping of population receptive fields (pRF) in these individuals using functional MRI revealed that in V2 and V3, Turner females show reduced pRF coverage of the periphery compared to control females. With this finding in mind, we performed a directed search for genes in V2 and V3 that correlated with eccentricity located on the X chromosome, with special attention for those on the short arm of the chromosome. Table S2 shows the complete list of genes from V2 and V3 that were correlated with eccentricity and were located on the X chromosome. In Fig 3, we highlight gene CXorf58 (Chromosome X open reading frame 58), which is not only located on the X chromosome short arm, but is also a gene whose mutations are known to result in Retinitis Pigmentosa, which is characterized by the loss of peripheral vision. Other notable genes were SLTRK4, directly involved in regulating neurite outgrowth and arborization, as well as RAI2, involved in cell growth. Both of these genes likely contribute to the CNF differences we observe in typical adult cortex, and their mutation likely has especially adverse impact on peripheral representations where cell density is already lower compared to foveal cortex.

Bibliography

- 1 Burt, J. B. et al. Hierarchy of transcriptomic specialization across human cortex captured by structural neuroimaging topography. *Nature Neuroscience*, doi:10.1038/s41593-018-0195-0 (2018).
- 2 Gomez, J., Zhen, Z. & Weiner, K. S. Human visual cortex is organized along two genetically opposed hierarchical gradients with unique developmental and evolutionary origins. *PLoS Biol* **17**, e3000362, doi:10.1371/journal.pbio.3000362 (2019).
- 3 Barone, P. D., C.; Berland, M.; Kennedy, H. Role of directed growth and target selection in the formation of cortical pathways: prenatal development of the projection of area V2 to area V4 in the monkey. *The Journal of Comparative Neurology* **374**, 1-20 (1996).
- 4 Hawrylycz, M. J. et al. An anatomically comprehensive atlas of the adult human brain transcriptome. *Nature*, doi:10.1038/nature11405 (2012).
- 5 Wandell, B. A. & Winawer, J. Imaging retinotopic maps in the human brain. *Vision Res* **51**, 718-737 (2011).
- 6 Benson, N. C. & Winawer, J. Bayesian analysis of retinotopic maps. *eLife* **7**, doi:10.7554/eLife.40224 (2018).
- 7 Wandell, B. A. & Winawer, J. Computational neuroimaging and population receptive fields. *Trends in cognitive sciences* **19**, 349-357, doi:10.1016/j.tics.2015.03.009 (2015).
- 8 Collins, C. E., Airey, D. C., Young, N. A., Leitch, D. B. & Kaas, J. H. Neuron densities vary across and within cortical areas in primates. *Proc Natl Acad Sci U S A* **107**, 15927-15932, doi:10.1073/pnas.1010356107 (2010).
- 9 Green, T. et al. X-chromosome insufficiency alters receptive fields across the human early visual cortex. *The Journal of Neuroscience*, doi:10.1523/jneurosci.2745-18.2019 (2019).
- 10 Stochholm, K., Juul, S., Juel, K., Naeraa, R. W. & Gravholt, C. H. Prevalence, incidence, diagnostic delay, and mortality in Turner syndrome. *J Clin Endocrinol Metab* **91**, 3897-3902, doi:10.1210/jc.2006-0558 (2006).
- 11 Gaudet, P., Livstone, M. S., Lewis, S. E. & Thomas, P. D. Phylogenetic-based propagation of functional annotations within the Gene Ontology consortium. *Brief Bioinform* **12**, 449-462, doi:10.1093/bib/bbr042 (2011).
- 12 Accogli, A. et al. A novel Xp22.13 microdeletion in Nance-Horan syndrome. *Birth Defects Res* **109**, 866-868, doi:10.1002/bdr2.1032 (2017).
- 13 Gomez, J., Natu, V., Jeska, B., Barnett, M. & Grill-Spector, K. Development differentially sculpts receptive fields across early and high-level human visual cortex. *Nature Communications* **9**, doi:10.1038/s41467-018-03166-3 (2018).
- 14 Dale, A. M., Fischl, B. & Sereno, M. I. Cortical surface-based analysis. I. Segmentation and surface reconstruction. *Neuroimage* **9**, 179-194, doi:10.1006/nimg.1998.0395 (1999).
- 15 Arnatkeviciute, A., Fulcher, B. D. & Fornito, A. A practical guide to linking brain-wide gene expression and neuroimaging data. *Neuroimage* **189**, 353-367, doi:10.1016/j.neuroimage.2019.01.011 (2019).
- 16 Smart, I. H. M. & McSherry, G. M. Gyrus formation in the cerebral cortex of the ferret. Description of the internal histological changes. *Journal of Anatomy* **147**, 27-43 (1986).
- 17 Kaschube, M. W., F.; Puhlmann, M.; Rathjen, S.; Schmidt, K.-F.; Geisel, T.; Lowel, S. The pattern of ocular dominance columns in cat primary visual cortex: intra- and interindividual variability of column spacing and its dependence on genetic background. *European Journal of Neuroscience* **18**, 3251-3266, doi:10.1046/j.1460-9568.2003.02979.x (2003).
- 18 Miller, J. A. et al. Transcriptional landscape of the prenatal human brain. *Nature*, doi:10.1038/nature13185 (2014).
- 19 Schleicher, A. Z., K.; Wree, A. A quantitative approach to cytoarchitectonics: software and hardware aspects of a system for the evaluation and analysis of structural inhomogeneities in nervous tissue. *Journal of Neuroscience Methods* **18**, 221-235 (1986).
- 20 Takahata, T., Shukla, R., Yamamori, T. & Kaas, J. H. Differential expression patterns of striate cortex-enriched genes among Old World, New World, and prosimian primates. *Cereb Cortex* **22**, 2313-2321, doi:10.1093/cercor/bhr308 (2012).

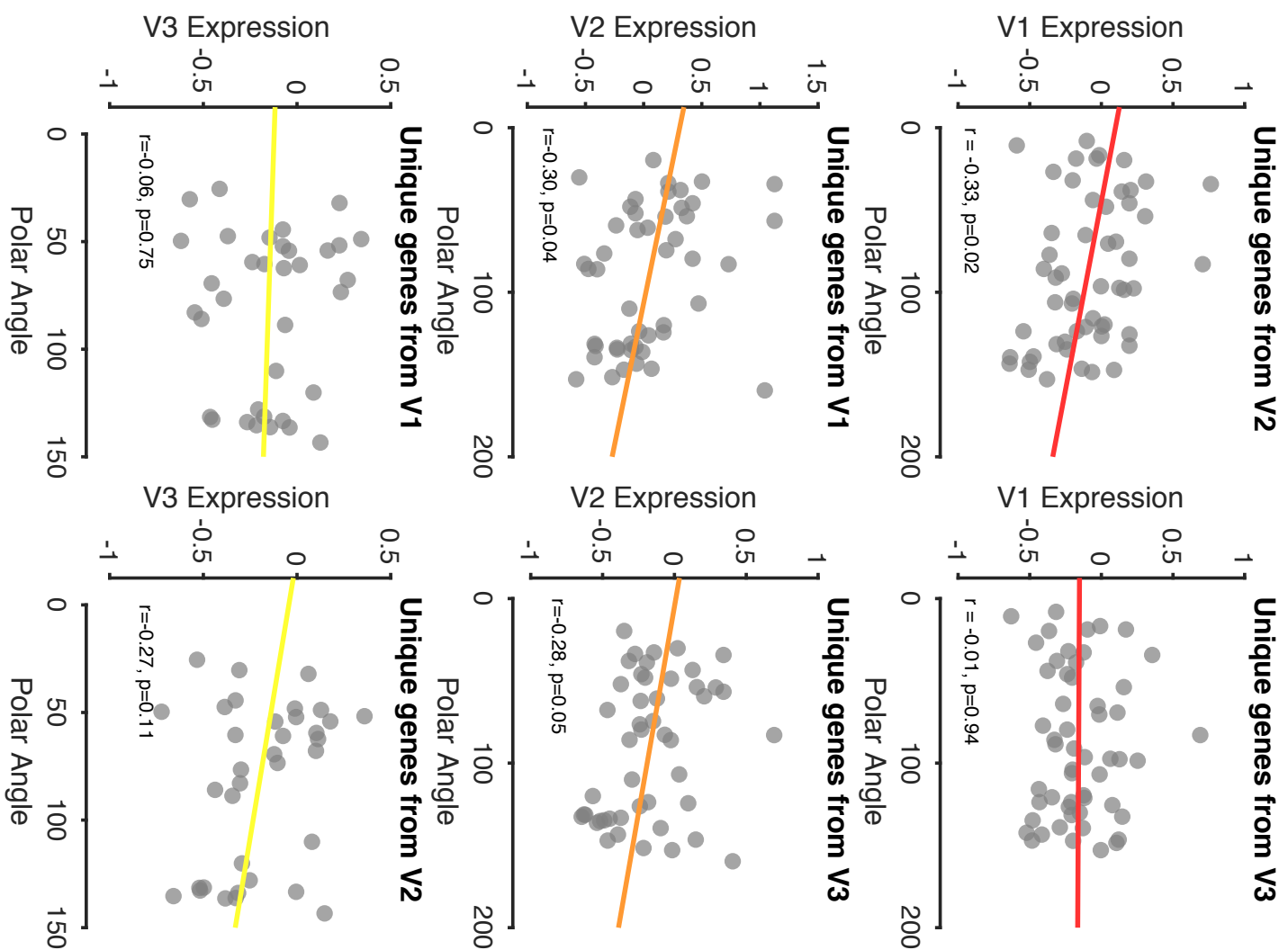


Supplementary Figure 1: Correlations between functional representation (polar angle and eccentricity) and the expression of positive and negative gradient genes. The mean expression of positive gradient genes within tissue samples are represented in pink dots, while the mean expression magnitude of negative gradient genes are shown in green. Pearson correlations and the resulting p-values are shown as inset text in each plot. Line of best fit for the positive and negative correlations are overlaid as gray lines. For each gradient, there are the following number of tissue samples: V1 (n=54), V2 (n=47), V3 (n=35). **(a)** Polar Angle. **(b)** Eccentricity.

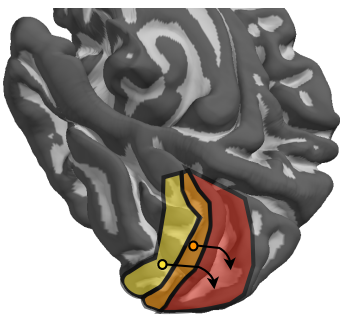
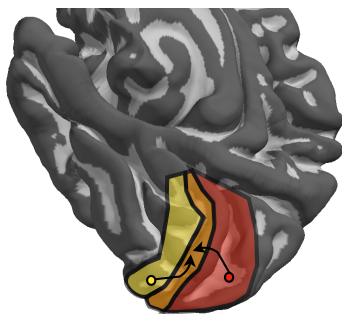
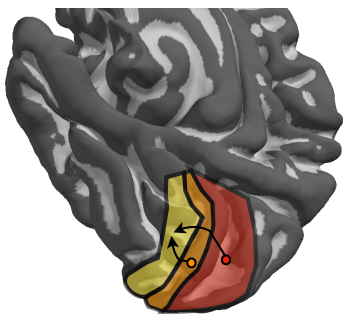


Supplementary Figure 2: Genes involved in hierarchical ordering of the ventral visual processing stream (inter-areal genes) are distinct from those correlated with eccentricity or polar angle (intra-areal genes). (a) Left: Dice coefficients summarizing the overlap of intra-areal genes in V1 through V3 with previously identified inter-regional genes that distinguish regions across the visual processing hierarchy. Right: The overlap of intra-regional genes of one visual area relative to the others. V1 and V2 share the most genes. Overall, the intra-regional genes are largely restricted to a given area. (b) Mean gene expression levels relative to polar angle (left) or eccentricity (right) values for the previously identified inter-regional genes belonging to the descending (top) and ascending (bottom) gradients ($-0.2 < r_s < 0.22$, p -values > 0.18). That is, there were two clusters of genes identified in Gomez, Zhen, & Weiner 2019 that varied linearly in expression level as one traversed the visual processing hierarchy (e.g., from V1 to ventral temporal cortex): one cluster that ascended in expression level (positive correlation) and one that descended (negative correlation) in expression level from early to late positions of the visual processing hierarchy. The expression of these inter-regional genes for either the descending (top) or ascending (bottom) gradient were not correlated with polar angle or eccentricity within areas V1, V2, or V3.

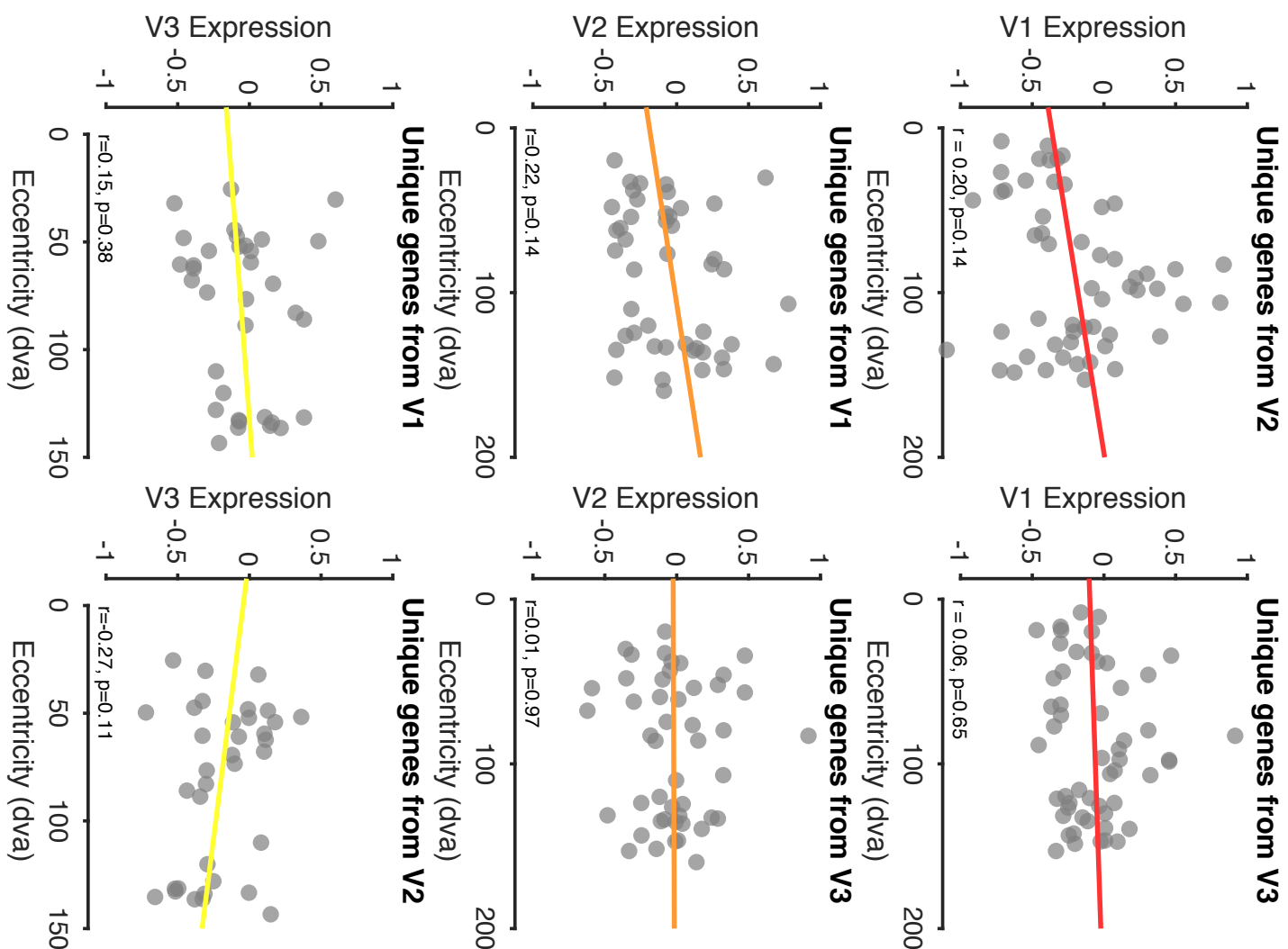
Negative Genes (polar angle)



Supplementary Figure 3: Correlations between polar angle and expression of negative genes from neighboring field maps. Polar-angle-correlated genes from each field map, while slightly overlapping, were largely a unique set of genes for each field map. To test whether the expression of genes from neighboring field maps were correlated with polar angle in the left out map, we took, for example, the genes from V2 and V3 correlated with polar angle, removed the overlapping genes that were correlated with polar angle in V1, and then correlated the mean expression of the remaining set of genes with polar angle in V1. The line of best fit is shown in each plot, and the resulting Pearson and p -values are inset as black text. Each gray circle is a tissue sample within a given field map.

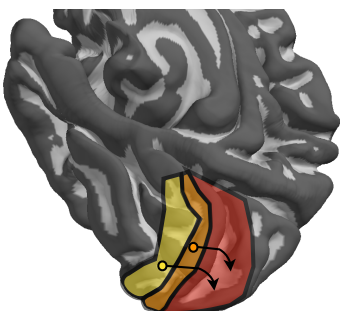
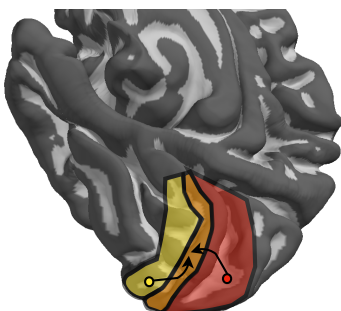
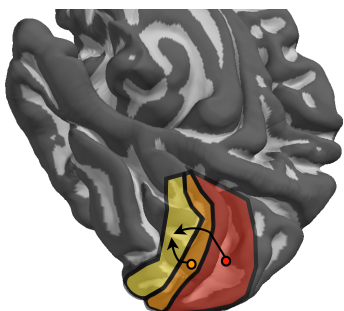


Negative Genes (eccentricity)

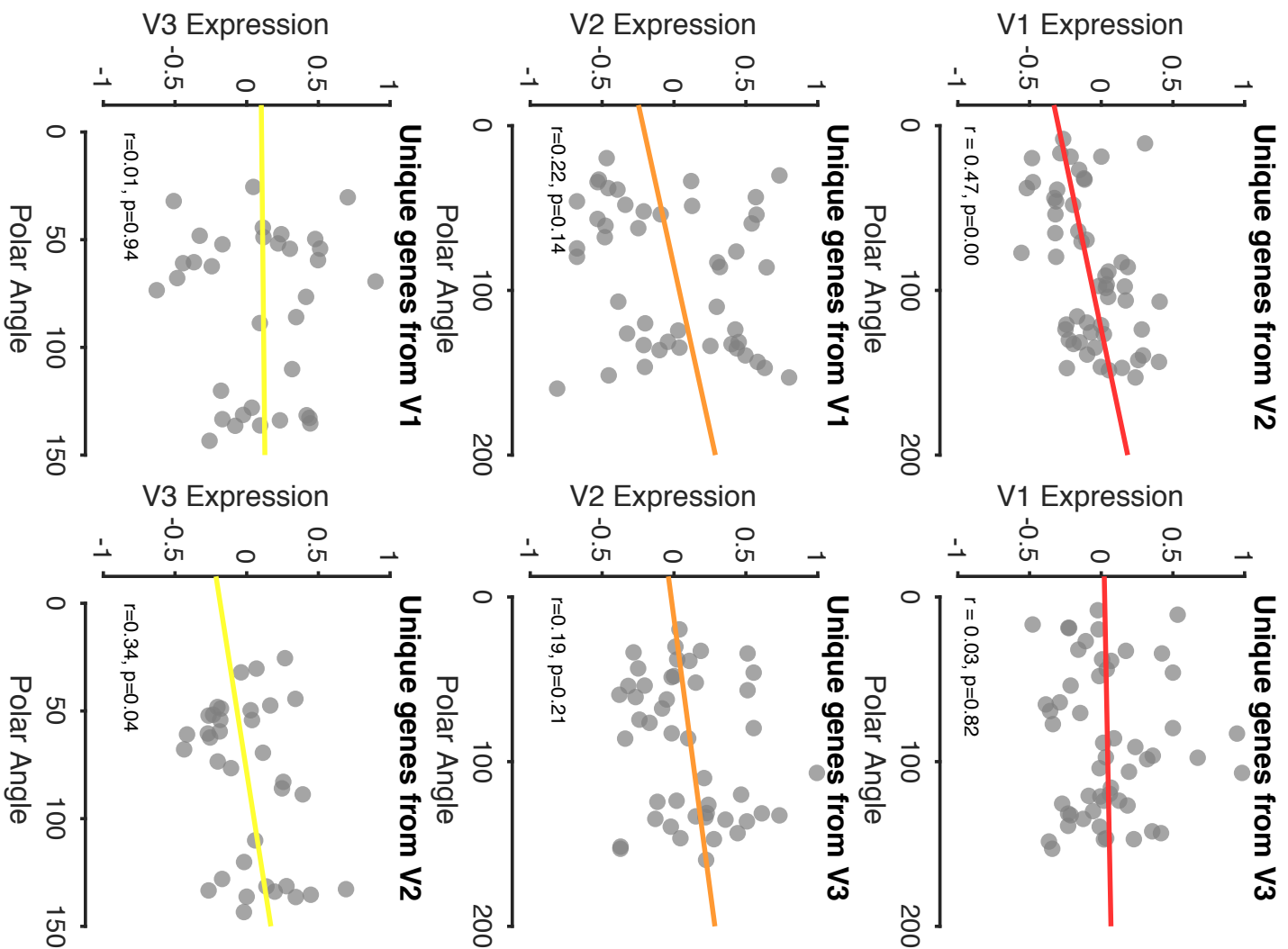


Supplementary Figure 4: Correlations between eccentricity and expression of negative genes from neighboring field maps.

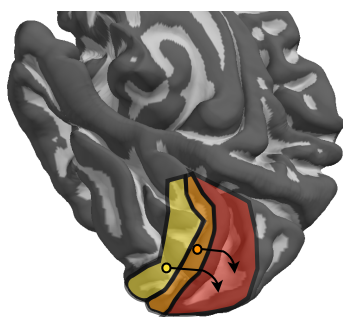
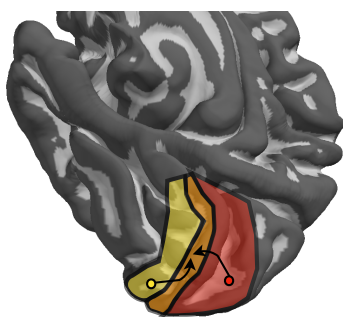
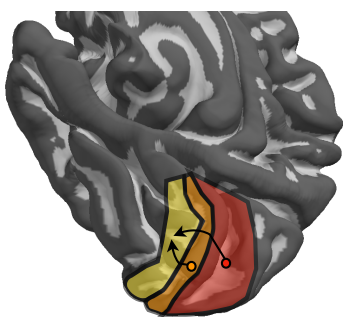
Eccentricity-correlated genes from each field map, while slightly overlapping, were largely a unique set of genes for each field map. To test whether the expression of genes from neighboring field maps were correlated with eccentricity in the left out map, we took, for example, the genes from V2 and V3 correlated with eccentricity, removed the overlapping genes that were correlated with eccentricity in V1, and then correlated the mean expression of the remaining set of genes with eccentricity in V1. The line of best fit is shown in each plot, and the resulting Pearson and p-values are inset as black text. Each gray circle is a tissue sample within a given field map.



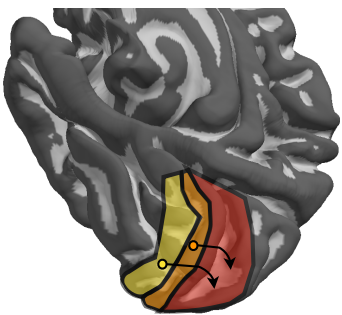
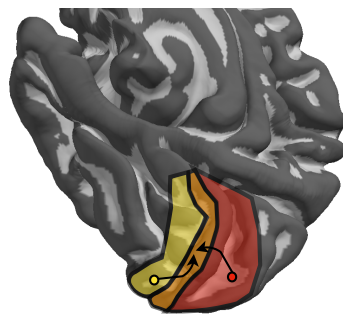
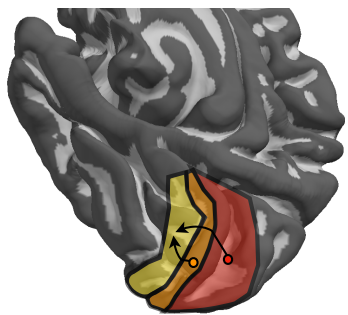
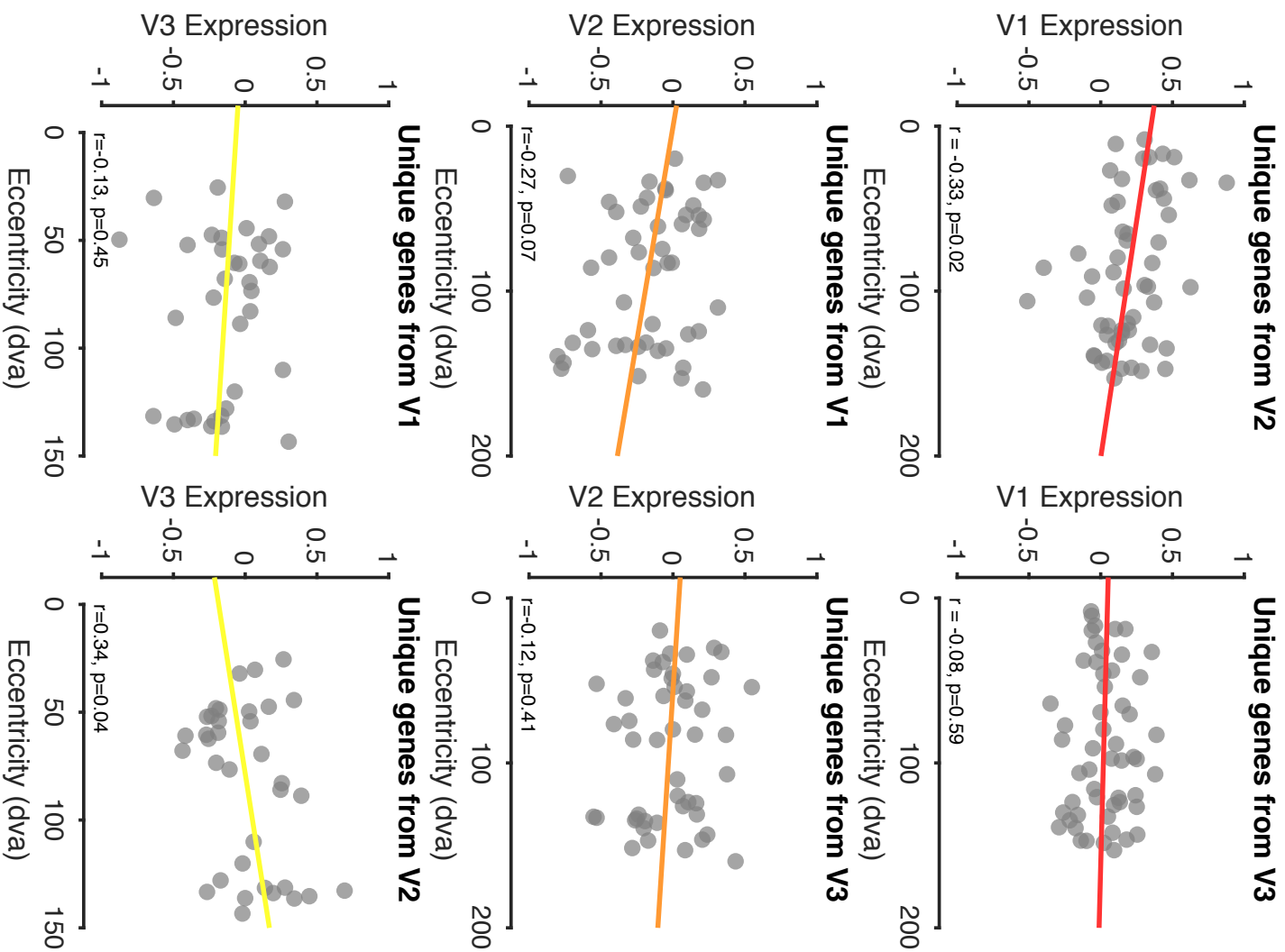
Positive Genes (polar angle)



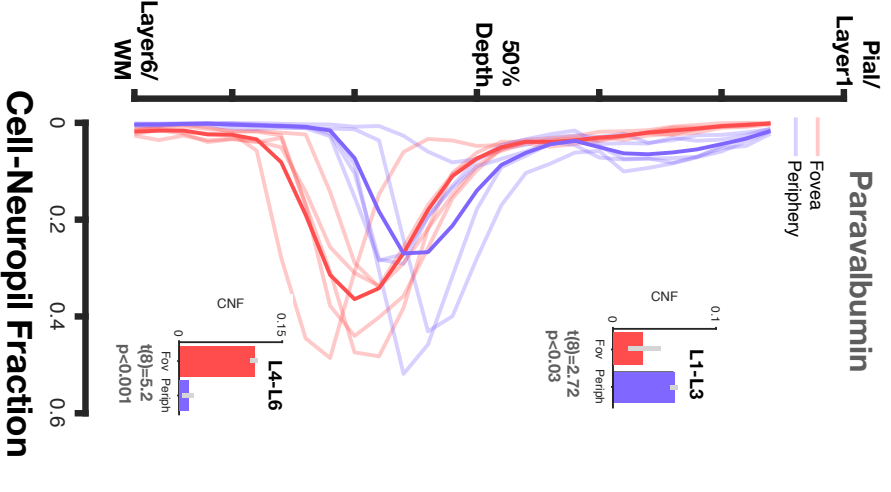
Supplementary Figure 5: Correlations between polar angle and expression of positive genes from neighboring field maps. Polar-angle-correlated genes from each field map, while slightly overlapping, were largely a unique set of genes for each field map. To test whether the expression of genes from neighboring field maps were correlated with polar angle in the left out map, we took, for example, the genes from V2 and V3 that were correlated with polar angle, removed the overlapping genes that were correlated with polar angle in V1, and then correlated the mean expression of the remaining set of genes with polar angle in V1. The line of best fit is shown in each plot, and the resulting Pearson and p-values are inset as black text. Each gray circle is a tissue sample within a given field map.



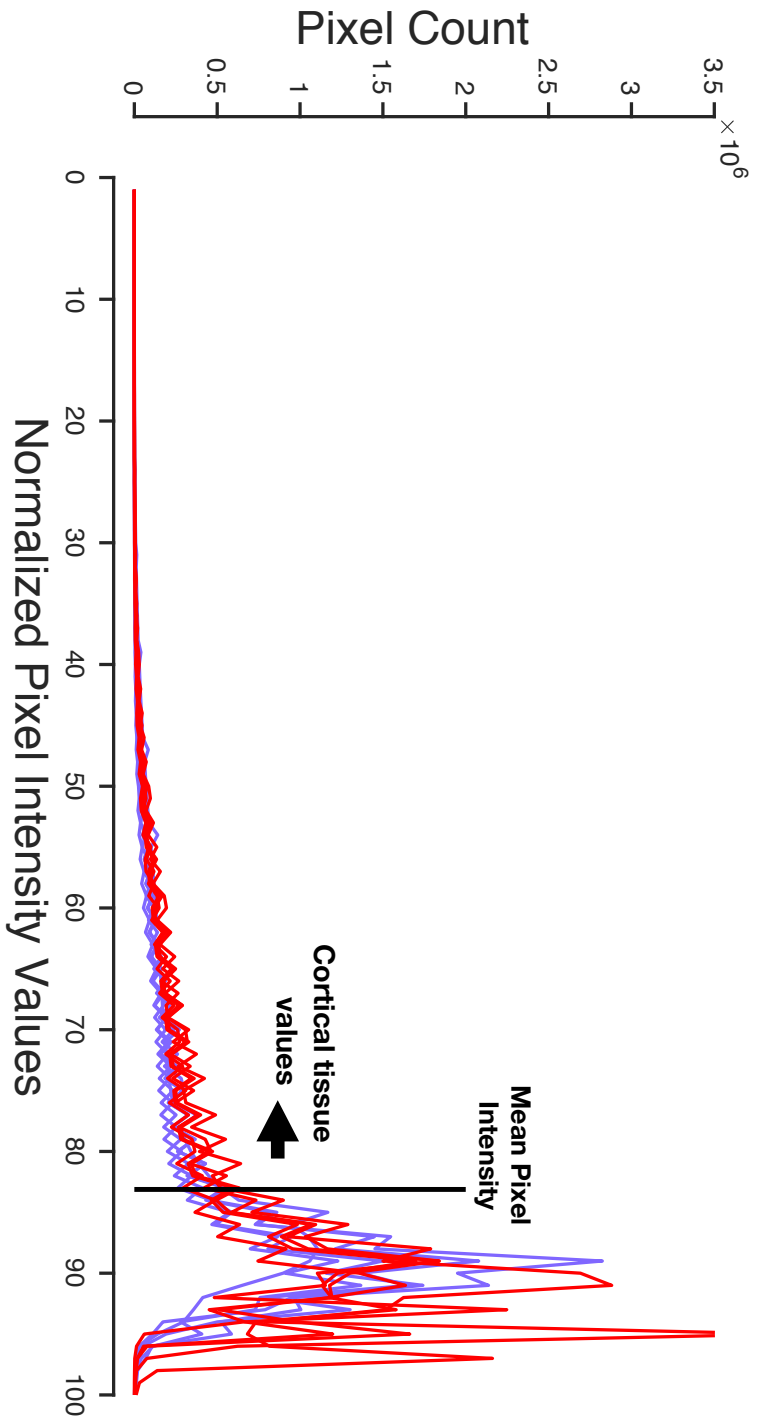
Positive Genes (eccentricity)



Supplementary Figure 6: Correlations between eccentricity and expression of positive genes from neighboring field maps. Eccentricity-correlated genes from each field map, while slightly overlapping, were largely a unique set of genes for each field map. To test whether the expression of genes from neighboring field maps were correlated with eccentricity in the left out map, we took, for example, the genes from V2 and V3 that were correlated with eccentricity, removed the overlapping genes that were correlated with eccentricity in V1, and then correlated the mean expression of the remaining set of genes with eccentricity in V1. The line of best fit is shown in each plot, and the resulting Pearson and p-values are inset as black text. Each gray circle is a tissue sample within a given field map.



Supplementary Figure 7: Differential presence of paravalbumin between foveal and peripheral visual cortex. CNF contours stained for Paravalbumin interneurons. We find that paravalbumin varies significantly between foveal and peripheral V1, with lower CNF in layers L4-L6 of peripheral cortex, and higher CNF in superficial layers (L1-L3). This analysis was conducted to verify that foveal and peripheral slices of V1 did not always vary by a global mean shift (potentially reflecting processing biases from AHBAl).



Supplementary Figure 8: Histograms of pixel values from foveal and peripheral Nissl stains of human tissue. To ensure that our chosen threshold for the BrainWalker CNF analysis was not impacting our results, we plotted the histogram of all pixel values from the foveal (red) and peripheral (purple) Nissl-stained slices from the AHBA. Higher values on the x-axis represent brighter pixels, with the large peaks from around $x=85$ to $x=100$ corresponding to the white background of the images, which represent the slide on which the tissue was mounted. The mean pixel intensity (the threshold used for the CNF analysis) is shown with a solid black line. The reader can appreciate that at the entire meaningful range (>60) of the lower intensity values below the mean corresponding to cortical tissue, foveal slices (red) show higher values than peripheral (purple) slices.

Supplementary Table 1: Genes correlated with eccentricity. Positively correlated genes are shown in orange, negatively correlated in blue. The top 1% of genes (ranked by -log of p-value) is shown for each field map.

V1 (Eccentricity)	V2 (Eccentricity)	V3 (Eccentricity)	V1 (Eccentricity)	V2 (Eccentricity)	V3 (Eccentricity)
ABCC1	ABCC1	A1CF	ABHD6	AARS2	ABHD4
AC007743.1	AC020663.1	ABCA6	AC005041.9	AC139099.1	AC010982.1
AC018865.8	AC068353.1	ABCC2	AC034236.3	ADAMDEC1	AC015936.3
AC022498.2	AC091878.1	AC007952.2	ACRV1	AGAP11	AC024270.1
AC068353.1	AC100803.1	AC018755.8	ACSL5	AMHR2	ADH1C
AC134312.1	AC112641.2	AC091878.1	ADAMTS16	ANP32A	ADIG
ACPT	ACTRT2	ADCY1	AKAP3	AP006285.4	ADRA1A
ADAMTSL5	ADAM23	AFAP1	ANGPT2	ASB14	AKIRIN2
ADD2	ADCY1	AFF1	ANKS6	ATAD3C	AP001372.1
ALG2	ADCYAP1	ALS2CR11	ARHGEF17	AVP	APOPT1
ANKLE1	ADRA1D	ANKRD34C	ARL6IP5	B4GALT1	ASPG
ANKRD20A7P	ALKBH8	ARHGEF1	ARL8A	BEST4	BCAP29
ANKRD34C	ANKRD34C	ASPM	ARMC7	BPNT1	BCHE
ARHGAP29	ARC	ATP1B1	ARMCX6	BTN3A1	BDKRB2
ARID1B	ARHGAP20	ATP6V1G2	ARRDC2	BUD13	BNIP1
ARID3A	ARSB	ATXN3	ATF3	C11orf53	C10orf107
BIRC6	ASAP1	BBS7	B2M	C11orf82	C18orf51
BMPER	ASGR1	BEGAIN	BACE1	C12orf48	C1orf187
BSND	ASH1L	BIRC6	BACE2	C15orf43	C1orf93
BTBD11	ASPSCR1	BMPER	BTN3A1	C15orf53	C2orf28
BTC	ATG9B	C16ORF52	BVES	C17orf89	C3orf70
BUB1B	BDNF	C16orf78	C10orf81	C1orf122	C5ORF27
C11orf84	BIRC6	C16orf92	C11orf53	C1orf168	C6orf72
C14orf4	BMPER	C22ORF45	C12orf48	C1orf194	C7orf10
C1orf135	BTBD11	C3orf18	C14orf91	C1orf92	C8orf71
C2orf54	C10orf72	C3orf35	C19orf18	C6orf118	C9
C3orf59	C12orf68	C4orf22	C19orf69	C6orf195	CARHSP1
C6ORF141	C13orf18	C7orf62	C1QTNF6	C6orf94	CATSPER2P1
C8A	C13orf44	CABC1	C21orf37	C6orf97	CATSPERB
C9orf71	C17orf39	CADPS	C5orf52	C9orf163	CCDC148
CAMK4	C17orf80	CALML4	C6orf48	C9orf96	CCDC21
CASKIN1	C17orf90	CALML5	C9orf117	CAMP	CD63
CBLN4	C1orf109	CD163L1	CARD18	CARD18	CDAN1
CCDC85B	C4orf22	CD164L2	CBR1	CASS4	CDH9

V1 (Eccentricity)	V2 (Eccentricity)	V3 (Eccentricity)	V1 (Eccentricity)	V2 (Eccentricity)	V3 (Eccentricity)
CD276	CAMK4	CD300LB	CCDC102B	CBWD6	CLCA3P
CHIC1	CBLN4	CDH20	CCDC150	CCDC21	CLEC18A
CHML	CCDC144NL	CDH23	CCDC53	CCDC74B	CLEC1A
CHST7	CD276	CDKL4	CD22	CCDC90A	CLNS1A
CITED2	CDH12	CDS1	CDH26	CCRL1	COIL
CLDN12	CDH23	CEACAM7	CETP	CCT6P1	CPA2
CNKS2R	CDH7	CELA2B	CFB	CDH26	CXorf58
COL4A1	CDK5R1	CGB2	CHI3L2	CFB	CYB5B
CRH	CEBPG	CLCF1	CHST6	CFL1P1	CYP2C9
CYB561D1	CHAC2	CLDND2	CLDND1	CHI3L2	CYP4Z2P
DAB1	CHST8	COASY	CLEC2A	CILP	DAB2
DNAJB13	CITED2	COL4A3	CNN2	CRYBA1	DAZAP2
DTX4	COL23A1	COX10	COMM3	CXorf58	DFFA
DUSP	COL5A2	CRHR2	CPB1	CYP4B1	DHODH
DUSP6	CRH	CRTC1	CPSF2	DCAF8L2	DHX58
EGR3	CRTC1	CTRL	CRYBA1	DDA1	DIRC2
EIF2A	CRYBB1	CTSZ	CSRP2	DDX10	DNASE1
ELANE	CS	DCLK1	CUTA	DDX50	DSE
ELOVL3	DBX1	DIRAS1	CYB5R2	DEFB113	EFHB
ENPP5	DIRAS1	DLAT	CYR61	DEFB123	ERMAP
ENTPD7	DLEU7	DOK3	DBNDD2	DIRC1	EYA1
ERVW-1	DNAJB5	E2F2	DDX43	DNASE1L3	FADD
ETV3	DPP6	E2F8	DEFB113	DRD3	FADS2
F2RL3	DTX4	EDEM3	DEPDC7	EDA	FAM108A5P
FAM171A2	DUSP6	EIF3A	DMBT1	EEF1A1P9	FAM110C
FAM190A	DUX4L15	EME1	DNASE1L3	EFCAB11	FAM111A
FAM53A	EGFL7	EMID2	DUOX1	ESF1	FAM23A
FOXA3	EID3	EPB41L5	ECM2	ESM1	FAM75C1
FRG2C	ELAVL4	FAM131C	EIF4ENIF1	EYS	FASLG
FRMD6	EMB	FAM166A	ERBB3	F11R	FER1L6
FXYD2	ENPP5	FBXO16	FAM112A	FAM120AOS	FIS1
G0S2	ENTPD7	FCF1	FANCL	FAM129A	FLJ30679
GABRB2	EPHA4	FCRL1	FBP2	FAM160A1	FLJ37396
GABRG3	EPN1	FGF20	FCRL3	FAM53C	FMO9P
GALNT5	EXTL3	FLJ37201	FLNB	FDPSL2A	FOXD3
GJB5	FAM104A	FLJ42627	FOLH1B	FEZF1	FOXF2

V1 (Eccentricity)	V2 (Eccentricity)	V3 (Eccentricity)	V1 (Eccentricity)	V2 (Eccentricity)	V3 (Eccentricity)
GLTPD1	FAM201B	FOXD4L4	GAGE6	FGA	GAL3ST2
GMEB2	FBXL19-AS1	FOXE3	GALNTL2	FLJ44635	GALNT10
GPR135	FOSB	GABRA1	GEN1	FLYWCH2	GCNT2
GPR156	FSTL4	GAL3ST3	GMPR2	FOXB1	GLOD4
GRIP1	FTSJ2	GALNT8	GNL3	GCSH	GNG10
GRM2	FUT11	GPA33	GNRHR2	GHSR	GPC6
GRM7	GABRB2	GPR157	GOT1L1	GIMAP2	GUK1
H2AFB2	GABRD	GPR26	GP6	GLTPD2	GYG2
H2AFY2	GAL3ST3	GVINP1	GPR18	GOT1L1	H3F3B
HCN3	GFRA2	HAOO	GPX8	GRIN3B	HEXA
HCRTR1	GJB5	HCN1	H3.Y	GSG2	HEY1
HCRTR2	GLCE	HCRTR1	HHLA3	HAUS8	HFM1
HDAC9	GLT25D1	HERC6	HOXC10	HLA-J	HLA-DQA1
HIST1H2AE	GPR158	HIVEP1	HSPA1A	HMGN2P15	HNRNPR
HIST1H3D	GRASP	HIVEP2	IGFBP1	HMHB1	HYI
HIST1H4K	GRIP1	HPX	IL15	HMX3	IL24
HIST4H4	GRM2	HS6ST2	IL1RL1	HNRNPA1P12	IL4R
HLA-DPB2	GRM7	HSD11B2	IL24	HOXC4	IMPDH2
HLF	H2AFB2	HSF1	IL4R	HTA	ISOC1
HOXC11	HDAC8	HSPA4L	INHA	IFI27	JUN
IPMK	HIST1H1E	HUNK	ITGA8	IFitm3	KHDRBS2
IPO4	HIST1H3F	HYLS1	ITIH5	IFNA1	KLRC3
IRF1	HIST1H4F	IGF2BP1	KIF7	IFT74	LACTB2
IRX3	HIST1H4J	IHH	KLHL4	IL24	LCN12
KCNA6	HIST1H4K	IL7R	KRT10	IL4R	LETM1
KCNB2	HIVEP2	ITGA11	KRT8P45	IQSEC2	LGI4
KCNG2	HTR3B	JMY	LACTB2	ISX	LIG1
KCNG4	HTR5A	KBTBD8	LAYN	ITGA1	LINC00471
KCNH5	INA	KIAA0408	LIPA	ITGB2	LOC100128009
KCNJ14	IP6K1	KIAA1009	LIPJ	ITIH5	LOC100131510
KCNJ16	JMJD5	KLHL26	LOC100130262	IVL	LOC100292680
KCTD9P2	KCNA1	KLHL6	LOC100130344	KIF20A	LOC283861
KDELc2	KCNA6	LCE3C	LOC100130932	KRTAP19-8	LOC389787
KIAA1161	KCND3	LCN6	LOC100287869	LAMC2	LOC441204
KIAA1530	KCNG2	LGNN	LOC100289070	LINC00116	LOC642943
KIR3DL3	KCNH5	LHB	LOC100294396	LINC00608	LOC645212

V1 (Eccentricity)	V2 (Eccentricity)	V3 (Eccentricity)	V1 (Eccentricity)	V2 (Eccentricity)	V3 (Eccentricity)
KLC3	KCNS2	LILRB3	LOC653653	LIPJ	LOC645431
KRTAP1-4	KCTD8	LILRB4	LOC728533	LOC100130935	LOC729859
KRTAP22-1	KCTD9P2	LIN28B	LOC728673	LOC100131727	LOC731157
KRTAP4-5	KIAA0748	LINC00176	LOC728819	LOC100132658	LOH12CR1
LFNG	KIAA1161	LIPT1	LOC732272	LOC100133775	LSM5
LIN7C	KIAA1632	LOC100131471	LOXL4	LOC100287017	MAPK3
LINC00339	KLF9	LOC100289944	LRRIQ4	LOC100287090	MEX3A
LINC00545	KLHL11	LOC100290497	LTF	LOC100293158	MGC34034
LOC100131830	KRT16P2	LOC149837	MAK	LOC100294396	MIS12
LOC100133299	KRT18P55	LOC200726	MAMDC2	LOC285741	MMP2
LOC100287391	LGALS7	LOC282997	MCM2	LOC388630	MRPL24
LOC100289632	LHFPL2	LOC388849	MGC12916	LOC441124	MS4A15
LOC100291206	LIG3	LOC401052	MITF	LOC442293	MTF1
LOC100291630	LINC00340	LOC440461	MORC4	LOC493754	NECAP2
LOC284072	LINC00473	LOC645944	MS4A6A	LOC550643	NEK11
LOC645431	LIPT1	LOC728613	MYOT	LOC554207	NUDT21
LOC652614	LOC100132364	LYVE1	NANO GP8	LOC642103	OR10W1
LOC728056	LOC100133299	MDGA2	NDE1	LOC650095	OR13C3
LOC728566	LOC100289550	MED23	NEK3	LOC728392	OR13H1
LONRF3	LOC100291124	MGC16025	NENF	LOC728673	OR2H2
LRRK1	LOC652614	MIA3	NMB	LOC729046	OR51I1
LYN	LOC84989	MTDH	NMNAT1	LOC729739	OR5B3
MORN1	LRRC61	MYO5B	NSBP1	LRCH4	PARD3
MSX1	LRRC8D	NDFIP2	NUF2	LRRIQ4	PCBD2
MUCL1	LRRK1	NR1I3	OIP5	MAFG-AS1	PCDH21
MYD88	LYPD5	OR1L6	OMG	MCART6	PGPEP1
MYO1B	MAD2L1	OR51B5	OPALIN	MRGPRF	PHKG1
NANOS2	MAFF	OR5A1	OR10X1	MYPN	PLAC8L1
NAPRT1	MAL2	OR8J1	PADI6	NACAP1	POLR2I
NOTUM	MAP2K7	OSBPL3	PARD6G	NCR2	PON3
NRTN	MARCH11	PAG1	PARP3	NDUFS5P7	PPAT
OCLM	MCF2L-AS1	PCDHGB3	PARP4	NEUROG3	PPIL6
OPRD1	MKS1	PCSK4	PDE11A	NFYB	PRDX1
OR10V1	MMAA	PDC	PDE6B	NME3	PRRG3
OR13C8	NRTN	PDE10A	PEBP1	NOD1	PSG2
OR13H1	OLFM3	PDE7A	PHACTR4	OR5L2	PSIP1

V1 (Eccentricity)	V2 (Eccentricity)	V3 (Eccentricity)	V1 (Eccentricity)	V2 (Eccentricity)	V3 (Eccentricity)
OR1N1	ONECUT3	PGC	PI16	ORM1	PUF60
OR2A14	OPRD1	PGR	PIGT	PABPC3	QPRT
OR2H2	OR2M5	PLCL2	PIWIL3	PARP4	RAB36
OR4D6	OSBPL10	PLEKHG6	PKD1L3	PCGF2	RAD54L
PABPC1L2B	PABPC1L2A	PNP	PLEKHG3	PGAM4	RDH8
PCDHB18	PAH	POU6F2	POPDC2	PHC3	REG1P
PCDHGA9	PCDHA5	PPM1E	PPIA	PIWIL3	RFT1
PCNXL3	PDE10A	PRRG4	PRKCH	POF1B	RGS21
PDE10A	PDP2	PRRT3	PROM1	PPBPL2	RHOA
PLA2G2D	PHF20	PRSS27	PRR20	PPIAL4G	RIT1
PLCH2	PI4K2A	PTK7	PTP4A2	PROM1	RNASE4
PLEKHF2	PIAS3	PUS10	PUS7L	PRRX1	RP11-169K16.9
PLVAP	PINX1	RAB3GAP2	QDPR	PTGIR	RP11-193H5.1
PPAPR5	PLCB4	RAI2	RBP3	PXDN	RP11-428G5.1
PPP1R3G	PPP1R13B	REEP5	RBP7	QKI	RP11-453F18_B.1
PPYR1	PRDM1	REG1B	RCL1	RAD51L1	RP11-535K1.1
PRB3	RASGRF2	RIMS3	RESP18	RAN	RPL13
PRDM1	RASSF5	RNASE2	RIBC2	RP1-10C16.2	RPL18
PRR5	RCSD1	RNF215	RNF183	RP11-193H5.1	RPS24
PRSS22	RG9MTD1	RP11-206L10.11	RNF39	RP11-349A22.5	RPS27L
RAPH1	RIMS3	RP13-254B10.1	RP11-115C21.2	RP11-379K17.4	RUNX3
RGR	SBK1	RP5-1187M17.1	RP11-45B20.3	RP11-475E11.5	S100A13
RHBDD3	SCN5A	SAMD5	RP11-537P22.1	RPL23AP82	SCPEP1
ROD1	SF3B4	SERINC4	RP3-486B10.1	RPL24	SDF2L1
RP13-254B10.1	SHQ1	SH3D20	RPL19P12	RPL32	SH2D4B
RP5-1187M17.1	SIDT1	SH3RF3-AS1	RPL23AP82	RPLP1	SHISA4
RPL32P3	SIPA1L2	SLAMF8	RSU1	RPS18	SIPA1
RPUSD1	SLC2A6	SLC16A3	SCGB1D4	S100A10	SIX2
S100A5	SLC37A2	SLC17A9	SDCCAG3P2	SEMG2	SLC22A24
SARDH	SLITRK4	SLC37A2	SEMA3C	SERBP1	SLC27A5
SBF1P1	SNX12	SLC4A9	SGK1	SESTD1	SLC6A13
SCN5A	SPATS2	SLC7A5P2	SH3BP4	SET	SLC6A2
SENP8	SPIRE1	SLC9A1	SH3PXD2A	SH3BP4	SLC7A9
SERTAD1	ST8SIA5	SLFNL1	SLC26A9	SIM2	SNRNP27
SHROOM3	STK40	SMPD3	SLC7A5	SLC22A18AS	SSX2B
SLC22A1	STS	SMPX	SLC9A9	SLC6A3	STK16

V1 (Eccentricity)	V2 (Eccentricity)	V3 (Eccentricity)	V1 (Eccentricity)	V2 (Eccentricity)	V3 (Eccentricity)
SLC22A13	STXBP5L	SNX25	SMOC1	SLC9A11	STMN4
SLC25A2	SUPT16H	SOST	SNIP1	SLC9A3	STXBP6
SLC36A1	SYT12	SSU72P8	SNX29	SNIP1	SULT1E1
SLC41A2	TAPBP	ST8SIA5	SPANXA1	SNPH	SYNJ2BP
SLC5A5	TBX21	TCF7L2	SPIC	SPEF2	TELO2
SNAI1	TCERG1L	TEX9	SPINK4	SPINK4	TEX264
SPDYE2	TCTN2	TNFRSF4	SPINT4	SPINT4	TLCD2
SPNS3	TM6SF1	TPTE2P1	SPTA1	SPOCK2	TM7SF2
STK3	TMEM25	TRAF5	TCFL5	SPRR1B	TMEM11
SYT12	TPBG	TRGV5	TMEM194B	STRA6	TMEM27
TCTN2	TSPAN5	TRIM21	TMEM206	SUMO2	TMEM47
TET3	TTC30A	TSKS	TNFAIP6	T	TMPRSS6
TIMP3	TUBA4B	TSPAN5	TRADD	TNF	TNFRSF10C
TNFRSF12A	UBASH3B	TTC39A	TRIM38	TRAM1	TRHR
TNFSF9	UBTD2	U2AF2	TTLL5	TRMT5	TSPAN4
TTC24	UHRF1	UGP2	TUBB1	TUSC1	TXNDC6
UBASH3B	USP10	UHRF1	TYMS	TXNL4A	UCKL1
UBTD2	UST	UHRF1BP1L	UBA6	UBOX5	ULK4
UHRF1	VIP	ZDHHC2	USP17L1P	UFM1	USP17L1P
WDR81	VWC2L	ZDHHC8	WDR49	UQCRHP2	USP18
XIST	WARS2	ZNF233	WNK1	USP54	VAT1
ZBTB5	ZBTB5	ZNF257	WTH3DI	VAX2	WAS
ZBTB7C	ZDHHC8	ZNF287	YWHAQ	WDR49	WDR6
ZDHHC8	ZNF35	ZNF354B	ZBED5	WTH3DI	WFIKKN2
ZNF239	ZNF385D	ZNF385A	ZDHHC15	XIRP1	YES1
ZNF385D	ZNF48	ZNF408	ZNF251	ZCRB1	YIPF7
ZNF697	ZNF567	ZNF700	ZNF311	ZNF727	ZBTB8B
ZNF772	ZNF74	ZNF823	ZNF705C	ZNF85	ZDHHC8P1
ZSCAN22	ZSCAN22	ZNHIT2	ZWINT	ZWINT	ZFP30

Supplementary Table 1 (continued): Genes correlated with polar angle. Positively correlated genes are shown in orange, negatively correlated in blue. The top 1% of genes (ranked by -log of p-value) is shown for each field map.

V1 (Polar angle)	V2 (Polar angle)	V3 (Polar angle)	V1 (polar angle)	V2 (polar angle)	V3 (polar angle)
AC008429.1	ABHD12B	ABHD14B	AC005077.3	ABCA7	AC002472.1
AC011346.1	AC008429.1	ABI1	AC005840.2	AC008537.3	AC087392.3
AC015871.2	AC013271.3	AC008073.2	AC103965.1	AC103965.1	ACTRT2
AC068181.1	AC063965.2	ACCN1	AC106739.1	ACAP3	AKAP11
AC092327.1	AC068181.1	ADAMTS9	ACAP3	ACLY	ANXA9
ACOT6	AC084209.1	ADH1C	ACHE	ACTRT2	AP3B1
ACRV1	ACOT6	AKIRIN2-AS1	ACIN1	AFF3	APOBEC3G
ADAD2	ACTA2	ALDOB	ADAM15	AHDC1	APPBP2
ADAMTS18	ACTG2	ANKRD1	ADD2	AMDHD2	ARFGEF1
ADCY10	ADAMTS2	ANXA2P1	AHDC1	ANKRD20A7P	ARMC3
AGTR1	AIM2	AOC3	ALKBH6	ARR3	RSB
ANKRD30A	ALPK3	ATG16L2	ANAPC13	ART5	ASB4
ATF3	ANGPT1	ATP5E	ANKRD24	ASH1L	ATF7IP
ATOH1	AOC3	ATP9B	AP1G2	ATXN3	BBX
BEND3	ASPN	BBS1	ARFGAP1	AURKC	BEND4
BSX	ATAD3C	BX248398.1	ATCAY	BANF1	BIRC6
BX255925.2	ATF7	C10orf10	ATP8B2	BCL11B	BPGM
C10orf53	ATP11C	C10orf104	ATXN1	BEND5	BZW1
C11orf34	AVIL	C10orf26	AURKA	BIRC6	C14orf119
C12orf48	C10orf68	C10orf68	BBC3	C10orf55	C19orf40
C14orf54	C15orf29	C11orf17	BCL6	C19orf52	C1orf156
C1orf180	C1orf229	C11orf57	C11orf63	C1orf190	C1orf55
C20orf29	C3orf15	C11orf75	C15orf38	C1orf68	C2orf61
C3orf44	C3orf20	C19orf73	C1orf190	C20orf144	C4orf37
C3orf48	C5orf25	C1orf204	C4orf22	C7ORF74	C5orf47
C5orf25	C6orf142	C1orf51	CACNA1A	CA12	C6orf153
C5orf52	C6orf15	C3orf31	CCDC136	CABP7	C6orf182
C6orf126	C7	C6orf26	CCDC142	CALHM1	C6orf91
C9orf117	CA13	C6orf48	CCDC57	CBX6	C7orf70
CARD18	CAPN14	C8orf59	CCDC66	CBX8	CALCB
CASR	CCDC102A	CAMK2A	CD276	CD276	CDC20
CCDC113	CCDC113	CAV1	CEND1	CDC2L1	CDC42BPG
CCDC135	CCDC18	CAV2	CEP152	CDC37	CDH20
CCDC140	CCDC46	CBR3	CERK	CDCA5	CDK7
CCDC27	CCDC52	CCDC102A	CHD6	CHD3	CDY2A
CCL16	CCL2	CCDC13	CHRD	COL23A1	CHEK1
CCR8	CD163	CCDC46	CIZ1	CREB3	CLCN3

V1 (Polar angle)	V2 (Polar angle)	V3 (Polar angle)	V1 (polar angle)	V2 (polar angle)	V3 (polar angle)
CD177	CD2AP	CDCA4	COL18A1	CTNNBIP1	CLDND2
CDH1	CDH18	CDKL3	CREBL1	CWC15	CRYBG3
CDNF	CDSN	CDKN2C	CRKL	DND1P1	CSNK2A1
CDRT15	CENPH	CFHR2	CUL7	DRD4	DCTN4
CETP	CENPK	CLIC1	CWC15	DSC2	DDC
CLRN3	CHMP4C	CLSTN1	CYB561D1	EGR3	DDI2
CRISP1	CHRNA3	CMTM2	CYP11A1	EMX2OS	DNAH9
CXCL11	CHRNA6	CNN1	DAXX	ERBB2	DOCK1
CXCL9	CLUL1	CNPY2	DCX	F7	DOCK2
CXXC4	COL13A1	CNTLN	DNAJC11	FAM129C	DSC2
CYAT1	COL14A1	COL1A1	EBF4	FAM74A1	DTX4
CYLC2	COL1A1	COL4A2	ENSA	FEN1	E2F8
CYP3A5	COL4A2	CPA3	ERG	FITM2	EFTUD1
CYP4F24P	CPXM2	CPSF4	ERVV-1	FKBP8	ELOVL2
DCAF4	CSN3	CREB3L2	ETV3	FOXA3	EVX2
DDX28	CXCL9	CTAG1B	FAM120B	G6PC3	FABP4
DDX43	CXCR3	CTBP1	FAM153A	GMCL1P1	FAM159A
DDX50	CYP4B1	CXCR3	FASN	GMIP	FAM166A
DIAPH3	DCAF4	CYR61	FKBP8	GNMT	FCF1
DNTT	DDX50	DGCR9	FLJ36848	GPR173	FCRL1
DUPD1	DEPDC1B	DHODH	FLJ42627	GRIPAP1	FGFR1
EN1	DGAT1	DIO3OS	FOXO3	GRPEL1	FNIP2
EPHA1	DHX29	DSE	FXYD2	GSX2	FOLR1
ESR2	DPT	ECSCR	GDAP2	H2AFB2	GALNT8
EVC	DSC1	EEF1A1P24	GEMIN7	HAAO	GRM8
FABP12	DSCAML1	EEF1A1P9	GJA9	HAND2	GRTP1
FAM120AOS	DSP	FAM111A	GLTPD1	HBBP1	GSC2
FAM124B	ECM2	FAM120AOS	GNPDA1	HDLBP	H2AFB1
FAM154A	ECSCR	FAM156A	GPR156	HEATR1	HCG26
FAM71B	ELL	FBLIM1	GPR20	HRG	HCP5B
FANCL	ELN	FBLN5	GPR21	HRH1	HIPK3
FCN2	EP400NL	FKBP10	GPRIN3	HSD17B1	HIST1H3A
FCRL2	EPHA1	FOLR4	GRPEL1	IGLL1	HIST1H3F
FER1L6	EPHA5	FOXK1	GTPBP5	IL22RA2	HIST1H4G
FOXI2	EYS	FOXL1	HDAC8	IL26	HIST1H4J
FRMD3	FAM129A	FRMD3	HIST1H1C	INO80B	HMMR
GAGE6	FAM186B	GNG11	HIST1H1E	KCNJ14	HOXA4
GATA2	FANCL	GNPDA2	HIST4H4	KIAA1161	HSPA5
GATA3	FBXO4	GPR120	HM13	KIAA1522	ICOSLG
GBP5	FHL5	GPX8	HMGB1P1	KIAA1530	IL15RA

V1 (Polar angle)	V2 (Polar angle)	V3 (Polar angle)	V1 (polar angle)	V2 (polar angle)	V3 (polar angle)
GJC3	FLNA	GRAMD4	HNRNPUL2	KIAA1549	INTS12
GLYATL1P2	FOXC1	HAUS7	HSPB6	KLC3	IRX2
GNAT1	FOXN1	HMCN1	IFIT3	KRTAP4-5	KAAG1
GOT1L1	FRZB	HMGN2	IGSF9	L1CAM	KCNA10
GRHL1	GAL3ST2	HNRNPA0	INTS4L1	LCE1F	KCNG2
GSN-AS1	GATA2	HYAL2	ITPR1	LCN1	KCNJ15
GUSBP10	GCET2	ICAM1	KCNC3	LEO1	KCTD9P2
HES2	GOT1L1	IFIH1	KCNJ14	LGALS7	KDEL2
HIST1H2BA	GPX8	IGFBP4	KCNJ8	LIG3	KIAA1324L
HPD	GTSF1	IGFBP7	KCTD1	LILRA3	KIAA1530
HPGD	GYS1	IQUB	KCTD8	LMOD2	KLF17
HSF2BP	HAUS8	ITGA8	KDM5D	LOC100287282	KPNA3
IFNK	HRC	ITGB1BP2	KGFLP2	LOC100288972	KRT76
IGHG4	ICAM2	JAG1	KIAA1522	LOC100289550	KSR1
IGSF2	IGHG2	KRTAP5-4	KIAA1530	LOC100290375	L1CAM
IL4	INO80D	LINC00307	KIR3DL3	LOC100291124	LDHAL6B
ISLR2	ITGA4	LINC00338	KLC3	LOC392264	LELP1
ITGB6	ITGA8	LOC100130700	KLC4	LOC400406	LGI1
KIF24	JAG1	LOC100130935	KRTAP4-5	LOC400419	LIG3
KLHDC7B	KCNU1	LOC100288618	KRTAP4-8	LOC400590	LINC00176
KRT13	KIAA0040	LOC100289058	KRTAP5-11	LOC643750	LINGO4
KRT23	KIAA1524	LOC100289525	LDB1	LOC646043	LMLN
KRT27	KLHL14	LOC100294396	LEO1	LOC727803	LOC100130000
KRT73	KLHL28	LOC440084	LOC100133299	LOC728056	LOC100130811
KRT77	LAMC3	LOC441204	LOC100287825	LOC728543	LOC100287987
LINC00421	LINC00421	LOC644397	LOC100288583	LOC728606	LOC100292160
LIPJ	LIPC	LOC653888	LOC100288972	LOC729887	LOC100294033
LOC100129852	LOC100129166	LOC729973	LOC100289550	LOC730183	LOC400406
LOC100130071	LOC100133862	LOC732327	LOC158696	LRRC4B	LOC402377
LOC100132738	LOC100287090	LOH12CR1	LOC284072	LRRTM2	LOC441528
LOC100133153	LOC100293158	LRRC47	LOC389842	LTB4R2	LOC651959
LOC100287487	LOC100293904	LSM5	LOC391334	MAML3	LOC728543
LOC100288908	LOC100507637	LTBP1	LOC392264	MAN1B1	LOC728853
LOC100291229	LOC439914	LTBP4	LOC401321	MAPK12	LRRC3
LOC220906	LOC440173	MDFIC	LOC727803	MAPT-AS1	LRRC45
LOC646762	LOC645722	MED17	LPCAT4	MEPE	MAP2K5
LOC646934	LOC646509	MGC24103	LRP1	MGC39584	MFI2
LOC653203	LOC646762	MORC2	LRRK1	MIXL1	MGC16025
LOC732327	LOC729839	MRGPRF	MUL1	MRPL50	MIR17HG
LY6G6D	LOC732327	MRPL43	MYD88	MVK	MMGT1

V1 (Polar angle)	V2 (Polar angle)	V3 (Polar angle)	V1 (polar angle)	V2 (polar angle)	V3 (polar angle)
LYZ	LRRC67	MSH5	NAPRT1	MYBPH	MTDH
MAGEA4	LTBP1	MSL3	NES	NANOS2	MTMR3
MAGEB1	MALT1	MTHFR	NEU4	NAPRT1	MTNR1B
MAGOH	MAP4K1	MTND4P12	NFATC2	NAT2	NAG18
MEP1A	MARVELD1	MUSTN1	NGRN	NLRP2	NALCN
MIA2	MCCC1	MYL12A	OGDH	NUCB1	NAPSA
MKI67	MCM2	MYL9	OLR1	OGDH	NAT8B
MKRN7P	MDFIC	NDUFB8	OR1N1	OR1K1	NCBP1
MMP1	MFAP4	NFYB	ORMDL3	OR2T5	NEBL
MMP20	MPP4	NLRP3	OTX1	OR4D5	NFATC4
MORC4	MRGPRF	NR4A1	PCIF1	OR4M2	NIPA2
MOV10L1	MYLK4	NRP1	PDE3B	OR5K1	NLGN2
MTNR1B	NANOGP8	OAZ1	PILRA	ORM2	NLRP10
MYLK3	NAP1L6	OGN	PINX1	PAPLN	NLRP4
NEK5	NDFIP2	OPN1SW	PIP5K1C	PCYOX1L	NR1I3
NKX3-2	NFYB	ORAI1	PLXNA3	PDE3B	OCRL
NUF2	NFYC	PARD6G	POMZP3	PIK3AP1	OR10A4
OR10G9	NHLRC2	PCDHB6	PP13	PIK3R2	OR2T33
OR1J1	NKAPL	PDCD2L	PPFIA4	PINX1	OR8J1
OR52V1P	NOBOX	PDGFRB	PPP1R3G	PLD2	ORM2
OR5J2	NSBP1	PDZRN3	PRB4	PLEC1	OVOL2
OR8J3	NT5C1A	PFAS	PRKACA	PLGLB2	PAX5
OR8K1	NUP188	PGM3	PRPF40B	PLXNA3	PBLD
OTC	OGN	PIP5K1A	PRR16	POLR3A	PCDHGA11
OTOR	OLFML2A	PKIG	PVT1	POPDC3	PCDHGA9
PADI6	OMD	PLAC8L1	RETN	POU2F2	PDK3
PAGE2B	OR5H1	PLAT	RHBDD3	PRAMEF7	PFKFB4
PAX8	OR5V1	PROCR	RHOBTB1	PRB4	PLA2G5
PDCL2	OTUD1	PRPS2	RHOBTB2	PRCC	POTEH
PDZK1IP1	PARD6G	PTGIS	RHOQP3	PRG3	POU1F1
PIK3C2G	PCDHB5	PXDN	RNF144A	PRSS22	POU2F3
PLUNC	PDE12	RAMP3	RNF157	PTCH1	PRAME
POM121	PGF	RANBP3	RNPS1P1	PVT1	PRAMEF25
PRG2	PIK3C2G	RASL12	RP11-440L14.1	RBM22	PRKG2
PSG11	PLN	RBPMS	RP5-1187M17.1	RCC1	PRO2012
PTGER4	PLS1	RP11-368J21.1	RPH3A	RN28S1	PTPN20B
RAD51AP1	POLR2A	RPL12	RPL23AP53	RNF219	PTPRD
RAD9B	PQLC3	RPL13	RPS6KA1	RP11-33B1.1	PUS10
RCVRN	PRPH2	RPL14	RPUSD1	RP11-440L14.1	RABL3
RHOXF1	PSG11	RPL15	RTL1	RP11-571M6.6	RALYL

V1 (Polar angle)	V2 (Polar angle)	V3 (Polar angle)	V1 (polar angle)	V2 (polar angle)	V3 (polar angle)
RIBC2	PTGIS	RPL23	RUSC1	RPL23AP53	RLN1
RNASE10	RAB17	RPL31	SAPS1	RPS6KA1	RP1-286D6.2
RP11-195F19.1	RAB7B	RPL31P11	SCARF1	RSL1D1	RP11-33B1.1
RP11-45B20.3	RAD21L1	RPL36A	SCARNA17	RWDD2B	RPN2
RP11-537P22.1	RASL11B	RPL38	SEPT6	SAPS1	RSC1A1
RP11-610O8.1	RP11-537P22.1	RPL4	SIPA1L2	SDC1	SERINC4
SAMD9	RP11-89K11.1	RPLP1	SLC26A8	SEMA6C	SF3B1
SCML4	RP5-820A21.1	RPN1	SLC6A17	SIGLEC8	SGPP1
SCNN1A	RRN3P1	RPP38	SMARCC2	SLC18A3	SHANK2
SH3BP4	SAMD9	RPS12	SPDYE2	SLC32A1	SLAMF9
SLC26A9	SCFD2	RPS17	SPTBN4	SLC4A9	SLC19A1
SLC35F2	SCNN1A	RPS19	SR140	SMCR7	SLC25A51P1
SPANXN4	SENP6	RPS20	SSX2B	SMPX	SLC26A2
SPATA19	SERPINF2	RPS21	STK11	SNCG	SLC2A3P1
SPINK4	SEZ6L	RPS25	STK19	SNX24	SLC36A4
SPRR2B	SGCA	RPS4Y2	STK40	SOAT2	SLC38A4
STK31	SIM2	RPS6	SYN3	SSTR5	SLFNL1
TDGF1	SLC13A4	RPS7	SYP	ST14	SNX30
TDO2	SLC24A4	RPSAP15	TADA3L	STK40	SPACA1
TDRD5	SLC25A30	RRN3P1	TAF3	TACC3	SPAG4L
TEKT5	SLC35A3	S100A11	TAOK2	TAF1	SPDYE2
TK2	SLC39A14	S100P	TCEAL2	TAF3	SPRR1B
TLR8	SMR3A	SCNN1A	TFPI	TAS2R40	TAS2R13
TMC5	SOX17	SDF4	TNFAIP1	TBX21	TBX21
TMEM200B	SPATA4	SERBP1	TNFRSF25	TCEAL1	TFDP3
TMEM75	ST8SIA6	SH3TC1	TNK2	TCEAL2	THEM4
TMPRSS4	STK31	SLC13A4	TNRC6A	TDRKH	TMC07
TNFAIP6	SUSD2	SLC19A3	TSPY26P	TERT	TMEM190
TNFRSF14	TAGLN	SLC2A1	UBL4A	TGFA	TMEM66
TPH1	TARP	SLC6A13	UHRF1BP1	THAP7	TMPRSS3
TRAT1	TEKT5	SNRPF	UNC13B	TMEM195	TNFSF15
TREML3	TEX9	SNX15	USP28	TMEM57	TNR
TRPC5OS	TFPI2	SSR4P1	VEGFA	TPBG	TPSAB1
TRPC6	TM6SF2	SUSD2	VSIG8	TRPM1	TRAF3IP2
TTY8	TMEM215	TGFBR2	VWC2	TSPY26P	TSPY1
TUBB1	TMEM79	TIMP3	WDR55	UMPS	TSPY26P
UPK1A	TNF	TMEM109	WWOX	URI1	TTC12
VCAM1	TRIM51GP	TMEM150A	ZHX3	WARS2	UBE4A
VIT	TTR	TMOD4	ZMAT3	WASL	UHRF1
VSX2	TTTY3B	TRAFF7	ZNF264	WWOX	WISP1

V1 (Polar angle)	V2 (Polar angle)	V3 (Polar angle)	V1 (polar angle)	V2 (polar angle)	V3 (polar angle)
WDR49	UGT2B10	TRAPPC2	ZNF385D	ZBTB5	XRCC2
XAGE1B	VSTM5	TSPAN1	ZNF485	ZDHHC8	XYLB
XIRP1	WNT2	TTC7A	ZNF513	ZFHX2	ZBTB33
ZBTB3	XIRP1	U2AF1	ZNF559	ZNF213	ZDHHC8
ZDHHC15	ZNF114	ULK4	ZNF585B	ZNF280B	ZNF300P1
ZFP92	ZNF2	WBSCR27	ZNF641	ZNF574	ZNF449
ZNF705C	ZNF304	WHAMML1	ZNF660	ZNF594	ZNF585B
ZNF732	ZNF597	XRRA1	ZNF704	ZNF704	ZNF594
ZNF90	ZNF799	ZAR1	ZNF749	ZNF710	ZNF772
ZWINT	ZP1	ZGPAT	ZNF787	ZNF771	ZSCAN21

Supplementary
Table 2

X chromosome genes correlated with eccentricity
CXorf58
DCAF8L2
EDA
FLJ44635
GYG2
H2AFB2
HDAC8
HS6ST2
IQSEC2
OR13H1
PABPC1L2A
PGAM4
POF1B
PRRG3
RAI2
SLTRK4
SMPX
SNX12
SSX2B
STS
TMEM47
WAS